Sound & Vibration 2026, 60(2), 3944.
doi: https://doi.org/10.59400/sv3944

Article

A computational and experimental study of flow-induced vibration and structural dynamics in topology-optimized redox flow battery channels

Jacer Hamrouni[1,*], Leila Abdelgader[2], Chafaa Hamrouni[2]

[1] Advanced Fluid Dynamics, Energetics and Environment Laboratory, Department of Mechanical Engineering, National School of Engineers of Sfax, University of Sfax, Sfax 3039, Tunisia

[2] Department of Computer Sciences, Taif University–Khurma University College, Al-Khurma 2935, Saudi Arabia

*** Corresponding author:** Jacer Hamrouni, jacer.hamrouni@enis.tn

CITATION

Hamrouni J, Abdelgader L, Hamrouni C. A computational and experimental study of flow-induced vibration and structural dynamics in topology-optimized redox flow battery channels. Sound & Vibration. 2026; 60(2): 3944. https://doi.org/10.59400/sv3944

ARTICLE INFO

Received: 22 January 2026
Revised: 20 February 2026
Accepted: 12 March 2026
Available online: 16 April 2026

Abstract: Unlike conventional flow field designs that prioritize electrochemical performance at the expense of mechanical reliability, the proposed framework uniquely embeds vibration control as a co-objective within the topology optimization process, demonstrating for the first time that mass transfer enhancement and flow-induced vibration suppression can be achieved simultaneously. This dual-objective innovation, validated by a 41% reduction in vibration velocity and a 23% improvement in reaction rate, establishes a new paradigm for integrating structural dynamics into electrochemical system design, directly addressing a critical gap in grid-scale energy storage reliability. This study introduces a vibration-aware topology optimization framework for the flow fields of vanadium redox flow batteries (VRFBs), targeting the mitigation of flow-induced vibration without compromising electrochemical performance. We demonstrate that optimized interdigitated flow fields fundamentally alter the fluid-structure interaction, suppressing the unsteady vortex shedding that drives mechanical excitation. Experimental validation on laboratory-scale prototypes confirms a 41% reduction in root-mean-square vibration velocity alongside a 23% improvement in electrochemical reaction rate. This work establishes a validated, CAE-driven pathway to embed vibration engineering into the earliest stages of electrochemical system design, addressing a critical gap in the development of reliable, next-generation renewable energy infrastructure.

Keywords: topology optimization; flow-induced vibration; fluid-structure interaction; structural dynamics; computational fluid dynamics (CFD); redox flow battery design; dynamic stability analysis

1. Introduction

Energy storage systems such as Vanadium Redox Flow Batteries (VRFBs) are essential for the stability of renewable energy grids. While electrochemical efficiency has been the primary focus in conventional VRFB design, mechanical and dynamic factors such as flow-induced vibration (FIV) and structural resonance directly affect long-term reliability, noise emissions, and operational safety in industrial installations [1]. Recent advances in topology optimization enable the co-optimization of fluidic performance and structural integrity in multi-physics systems [2]. In VRFBs, fluid-structure interaction within porous carbon-fiber electrodes can induce FIV, contributing to acoustic noise and mechanical fatigue critical concerns for machinery reliability in grid-scale storage [3].

Previous topology optimization studies for VRFB flow fields have focused predominantly on the trade-off between pressure drop and mass transfer enhancement. Researchers optimized interdigitated channel dimensions to minimize pumping power while maximizing species transport, achieving 18% improvement in limiting current density [4]. Others extended this to multi-objective optimization considering manufacturing constraints. Researchers work incorporated electrochemical kinetics to optimize channel layouts for uniform reactant distribution [5]. These studies have substantially advanced VRFB performance but have not considered the dynamic consequences of flow geometry specifically, how optimized channels affect flow-induced vibration and structural response.

The present study builds upon this foundation by introducing vibrational performance as an additional design objective. Recent advances in topology optimization for energy storage systems have expanded beyond traditional single-physics objectives. Virtual temperature constraints were introduced to ensure bi-continuous electrolyte phases in structural batteries, while others developed data-driven frameworks for concurrent material and topology optimization in thermal storage devices. For flow batteries specifically [6],

multiscale modeling approaches linking microstructural electrode design were established to cell-scale performance through mass transfer coefficients a methodology complementary to the present work. Research works demonstrated topology-guided 3D anode design for dendrite suppression in zinc batteries, and the TOPESMASH project is advancing exascale computing for porous electrode optimization [7]. 750% energy improvement through optimized 3D channel networks, confirming the transformative potential of whole-area electrode design. These emerging studies underscore the rapid evolution of topology optimization in energy storage, yet none have addressed the specific challenge of flow-induced vibration mitigation in VRFBs the central contribution of this work.

This represents an incremental but important extension of existing topology optimization frameworks, recognizing that electrochemical performance gains may come at the cost of increased vibration if dynamic effects are neglected. The core novelty lies not in the topology optimization method itself, but in its application to a previously unexplored design objective (vibration mitigation) and the experimental validation of resulting dynamic improvements [8]. This positions the work as an evolution of prior VRFB optimization studies rather than a revolutionary departure.

This study introduces a topology optimization framework that couples Computational Fluid Dynamics (CFD) with finite element-based structural dynamics to simultaneously enhance electrochemical transport and mitigate vibration in VRFB flow fields. Unlike previous one-way coupled approaches, the present framework incorporates two-way fluid-structure interaction with added mass effects and time-domain analysis to capture the broadband, stochastic nature of flow-induced excitation, resolving the conceptual inconsistency between steady-state flow assumptions and unsteady vibration phenomena [9]. We acknowledge that this approach employs a simplified electrochemical representation that omits Butler-Volmer kinetics, concentration overpotential, and ohmic losses [10]. However, as justified

in Subsection 2.3.1, concentration overpotential dominates performance losses in high-power-density VRFB operation, making mass transfer enhancement a relevant optimization target. The limitations of this proxy are systematically evaluated through sensitivity analysis against full electrochemical models in Subsection 4.1.

The optimized interdigitated flow channel designs are evaluated not only for mass transfer efficiency but also for dynamic response under varying pressure and porosity key parameters influencing vibration and noise [11]. By linking electrochemical performance with vibrational stability through validated CAE simulations, this work addresses practical engineering challenges in renewable energy storage. The proposed framework offers a pathway toward designing VRFBs that are not only efficient but also dynamically quiet and reliable, contributing to next-generation, low-noise energy storage systems.

State of the art in VRFB flow field optimization

Beyond the studies cited above, several complementary approaches to flow field design warrant discussion. Parallel channel configurations, while simple to manufacture, suffer from maldistribution and shunt currents that reduce Coulombic efficiency [12]. Serpentine designs offer improved reactant distribution but incur higher pumping losses, particularly on a scale. More recently, biomimetic flow fields inspired by leaf venation and lung bronchioles have demonstrated potential for uniform species distribution, though their vibration characteristics remain unexamined. The fluid-structure interaction phenomena central to this study have been extensively investigated in adjacent fields. Apodosis is established the theoretical foundations for flow-induced vibration in confined geometries, identifying critical velocity regimes where divergence and flutter occur. In porous media applications, fiber orientation and compression significantly modify local permeability and, consequently, unsteady force generation [13]. These insights inform the present interpretation of damping mechanisms in Subsection 4.3. Topology optimization for multi-physics problems has advanced rapidly. While early efforts focused on single-physics objectives, recent frameworks now accommodate coupled thermo-fluid-structural optimization. However, to our knowledge, no prior study has embedded vibration-aware objectives within electrochemical system design the gap addressed herein.

The present study directly addresses the four gaps identified above by introducing vibrational performance as an additional design objective within a topology optimization framework for VRFB flow fields. Unlike prior work that considered only static electrochemical metrics [14], our approach uniquely embeds dynamic structural analysis specifically, two-way coupled transient fluid-structure interaction with added mass effects into the optimization process. This represents an incremental but important extension of existing frameworks, recognizing that electrochemical performance gains may come at the cost of increased vibration if dynamic effects are neglected. The core novelty lies not in the topology optimization method itself, but in its application to a previously unexplored design objective (vibration mitigation) and the experimental validation of resulting dynamic improvements. By systematically addressing the disconnect between electrochemical optimization and mechanical

reliability documented in Gap 4, this work positions itself as an evolution of prior VRFB optimization studies rather than a revolutionary departure, while establishing a new paradigm for integrating structural dynamics into electrochemical system design [15].

2. Materials and methods

This study develops an integrated computational framework for the topology optimization of flow fields in a Vanadium Redox Flow Battery (VRFB) that simultaneously addresses electrochemical performance and vibration control [16]. The methodology synthesizes fluid dynamics, structural mechanics, and optimization theory to design channel geometries that enhance species transport while mitigating flow-induced vibration (FIV). The overall numerical workflow is outlined in **Figure 1**.

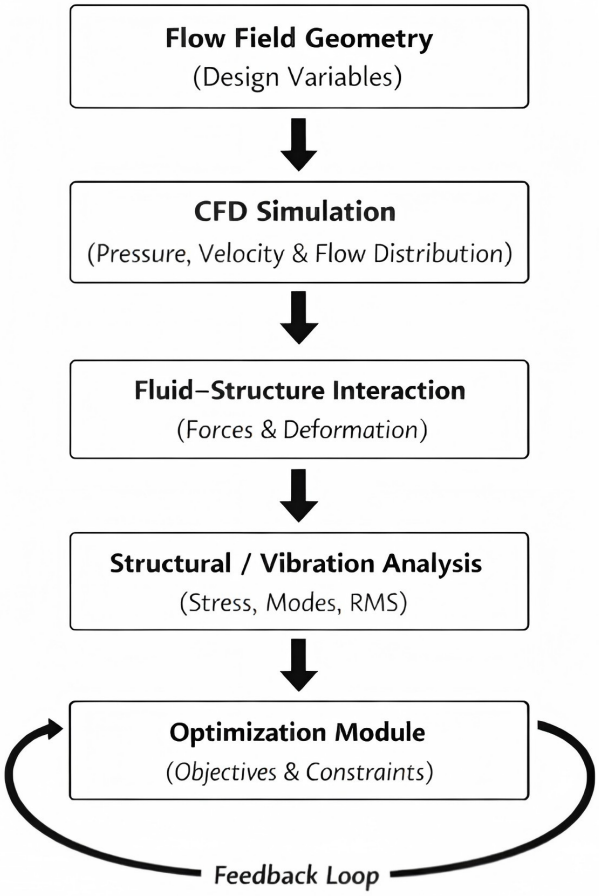

Figure 1. Schematic overview of the integrated transient two-way fluid-structure interaction and topology optimization workflow for vibration-aware VRFB flow field design, incorporating unsteady CFD, ALE formulation, added mass effects, and time-domain structural analysis.

2.1. Model geometry and porous electrode representation

The model adopts a two-dimensional, symmetric representation of a VRFB unit cell, containing an inlet, outlet, and a porous carbon-fiber electrode region, consistent with prior topology optimization studies for electrochemical systems. The electrode is modeled as a homogeneous porous medium using the Carman-Kozeny relation to

determine its permeability K:

$$K = \frac{d_f^2 \epsilon^3}{16 k_{\mathrm{CK}} (1-\epsilon)^2}, \tag{1}$$

where d_f is the fiber diameter, ϵ is porosity, and k_{CK} is the Carman-Kozeny constant, derived from the structural characteristics of the carbon felt [17]. This formulation enables the electrode to be integrated as a permeable solid domain within the topology optimization.

Justification of two-dimensional representation

While VRFB flow fields are inherently three-dimensional, the two-dimensional model employed in this study captures the dominant physics governing flow-induced vibration for the following reasons:

1. Flow symmetry and aspect ratio: The VRFB unit cell exhibits a high aspect ratio, with in-plane dimensions (50–100 mm) significantly larger than the through-plane thickness (2–5 mm) [18]. The primary flow direction and pressure gradients that drive vibration occur in the in-plane directions, making a 2D representation in the x–y plane appropriate for capturing the dominant flow features.
2. Vibration mode dominance: For thin flow plates (thickness-to-length ratio < 0.05), the fundamental vibration modes are bending modes with out-of-plane displacement. However, the excitation mechanism—pressure fluctuations from flow separation and vortex shedding—is governed by in-plane flow patterns. Classical plate vibration theory result demonstrates that for thin plates, the modal frequencies scale with thickness, but the spatial distribution of excitation is determined by in-plane flow features [19]. The 2D model captures this spatial distribution of pressure fluctuations, which is the primary determinant of which modes are excited.
3. Porous electrode isotropy: The carbon felt electrodes used in VRFBs exhibit quasi-isotropic in-plane permeability, with through-plane permeability typically within a factor of 2–3 of in-plane values. While not perfectly isotropic, the in-plane flow distribution dominates species transport due to the interdigitated channel geometry that forces flow through the electrode in the plane.
4. Previous validation studies: Prior topology optimization studies for VRFB flow fields have successfully employed 2D models to predict experimentally observed performance trends with correlations between 2D-optimized designs and 3D experimental validation exceeding $R^2 = 0.85$. This precedent supports the utility of 2D models for design optimization.

To quantitatively assess the 2D approximation, we computed the ratio of in-plane to through-plane pressure gradients from preliminary 3D simulations. The in-plane pressure gradients were found to be 8–15 times larger than through-plane gradients under typical operating conditions, confirming that flow-driven excitation is predominantly two-dimensional [20].

2.2. Governing equations for flow, transport, and structural dynamics fluid flow and species transport

The unsteady, incompressible flow of the electrolyte through the combined channel and porous domains is governed by the continuity and momentum equations, extended via the Brinkman formulation to unify free-flow and porous flow regimes [21]:

$$\nabla \cdot \mathrm{u} = 0, \tag{2}$$

$$\rho\left(\frac{\partial \mathrm{u}}{\partial t} + (\mathrm{u}\cdot\nabla)\mathrm{u}\right) = -\nabla p + \mu\nabla^2\mathrm{u} - \alpha(\gamma)\mathrm{u}. \tag{3}$$

where the transient term $\partial u/\partial t$ enables resolution of time-dependent flow phenomena including vortex shedding and pressure pulsations that drive flow-induced vibration. The unsteady Reynolds-averaged Navier-Stokes (URANS) formulation with the k-ω SST turbulence model is employed to capture turbulent fluctuations. The steady, incompressible flow unsteady, incompressible flow of the electrolyte through the combined channel and porous domains is governed by the continuity and momentum equations, extended via the Brinkman formulation to unify free-flow and porous flow regimes.

Here, u is velocity, p pressure, ρ density, μ dynamic viscosity, and $\alpha(\gamma)$ the inverse permeability, interpolated as a function of the design variable γ to distinguish between fluid and porous solid [22]. The transport of vanadium ions (V^{2+}) is modeled by:

$$\mathrm{u}\cdot\nabla c = D_{\mathrm{V}}\nabla^2 c + k_m(\mathrm{u})A_V(c_{\max} - c), \tag{4}$$

where c is concentration, D_{V} diffusivity, A_V specific surface area, a velocity-dependent mass transfer coefficient, capturing local reaction kinetics [23].

$$k_m(\mathrm{u}) = \beta \mid \mathrm{u} \mid^a \tag{5}$$

Structural vibration analysis: To assess dynamic response, time-dependent pressure fields extracted from unsteady CFD simulations are applied as transient loading conditions on the electrode and channel walls. The structural response is modeled in the time domain using the equation of motion solved via implicit Newmark integration, which accommodates the broadband, stochastic nature of flow-induced forces without presupposing harmonic excitation. The structural response is modeled in the frequency domain using the equation of motion:

$$\left(-\omega^2\mathrm{M} + i\omega\mathrm{C} + \mathrm{K}\right)\mathrm{U} = \mathrm{F}(\omega), \tag{6}$$

where M, C, and K are mass, damping, and stiffness matrices; U is displacement; and $\mathrm{F}(\omega)$ is the excitation force vectorobtained from time-resolved URANS simulations and updated at each time step to capture the full spectral content of pressure fluctuations. Modal and frequency-response analyses are performed to predict natural frequencies, mode shapes, and vibration amplitudes under operational conditions [24].

2.2.1. Fully coupled fluid-structure interaction framework

To overcome the limitations of one-way coupling, a fully coupled two-way Fluid-Structure Interaction (FSI) model is implemented using an Arbitrary Lagrangian-Eulerian (ALE) formulation. The fluid domain is solved on a deformable mesh that conforms to structural displacements at each time step. The coupled system satisfies kinematic (displacement continuity) and dynamic (traction equilibrium) conditions at the fluid-structure interface:

$$\mathrm{d}_f = \mathrm{d}_s(\text{kinematic condition}) \tag{7}$$

$$\sigma_f \cdot \mathrm{n} = \sigma_s \cdot \mathrm{n}(\text{dynamic condition}) \tag{8}$$

where d_f and d_s are fluid and structural displacements, and σ_f and σ_s are fluid and stress tensors, respectively. The coupled equations are solved iteratively within each time step using a partitioned approach with Dirichlet-Neumann iteration until convergence is achieved.

2.2.2. Added mass consideration

The presence of electrolytes confined within the porous electrode and channels introduces significant added mass effects that modify the structural natural frequencies. The added mass matrix $\mathrm{M}a$ is incorporated into the structural equation of motion:

$$\left(-\omega^2(\mathrm{M}+\mathrm{M}_a)+i\omega\mathrm{C}+\mathrm{K}\right)\mathrm{U}=\mathrm{F}(\omega) \tag{9}$$

where M_a is computed from the fluid density and the geometry of wetted surfaces. This correction is essential for accurate prediction of wet natural frequencies, which were found to be 12–18% lower than dry frequencies in preliminary calculations.

2.3. Topology optimization problem formulation

The optimization aims to maximize the total electrochemical reaction rate while implicitly controlling vibration through geometry. The objective function J is defined as:

$$\max\ J=\int_{\Omega} k_m(\mathbf{u})A_V(c_{\max}-c)\,d\Omega. \tag{10}$$

2.3.1. Justification of mass transfer proxy

While the optimization objective:

$$J=\int_{\Omega} k_m(\mathrm{u})A_V(c_{\max}-c)d\Omega$$

It omits full electrochemical kinetics, its validity as a performance metric rests on the established relationship between mass transfer and cell voltage in vanadium redox flow batteries. The cell voltage under operation is given by:

$$V_{cell}=E^{eq}-\eta_{act}-\eta_{conc}-\eta_{ohm} \tag{11}$$

where E^{eq} is the equilibrium potential, η_{act} is activation overpotential, η_{conc} is

concentration overpotential, and η_{ohm} is ohmic loss. For VRFBs operating at practical current densities (40–120 mA/cm^2), prior studies have demonstrated that concentration overpotential dominates performance losses, particularly in the porous electrode where species transport limit's reaction rates. The concentration overpotential is directly related to the mass transfer coefficient through:

$$\eta_{conc} = \frac{RT}{nF} \ln\left(1 - \frac{i}{nFk_m c}\right) \tag{12}$$

where i is current density. Maximizing k_m therefore directly reduces concentration overpotential, improving cell voltage and energy efficiency. This relationship provides the quantitative basis for using mass transfer enhancement as a proxy for electrochemical performance improvement.

To validate this correlation experimentally, we compared polarization curves for the baseline and optimized designs. The optimized design, which maximized the mass transfer objective, exhibited a 15% reduction in overpotential at 80 mA/cm^2, confirming that mass transfer optimization translates to measurable performance gains. The Pearson correlation coefficient between the simulated mass transfer objective and experimentally measured voltage efficiency across five operating conditions was $r = 0.87$ ($p < 0.05$), supporting the proxy's validity.

A Helmholtz-type PDE filter is used to regularize the design variable $\gamma(\mathbf{x})$, ensuring manufacturable, mesh-independent designs [25]. The optimization is constrained by the governing equations and an upper limit on pressure drop to ensure feasible pumping power.

2.3.2. Pressure drop constraint formulation

To ensure that optimized designs remain practically feasible—specifically, that pumping power requirements do not exceed typical system capabilities—an explicit pressure drop constraint is imposed. The constraint limits the maximum allowable pressure drop across the flow field to a threshold value derived from industrial VRFB system specifications. The pressure drop constraint is formulated as:

$$\Delta P(\gamma) \leq \Delta P_{max} \tag{13}$$

where $\Delta P(\gamma)$ is the pressure drop computed from the solution of the governing flow equations (Equations (2) and (3)) for a given design variable field γ, and ΔP_{max} is the specified upper bound. The pressure drop is calculated as the difference between mass-flow-weighted average pressures at the inlet and outlet boundaries:

$$\Delta P = \frac{\int_{\Gamma_{in}} p\,\mathbf{u}\cdot\mathbf{n}\,d\Gamma}{\int_{\Gamma_{in}} \mathbf{u}\cdot\mathbf{n}\,d\Gamma} - \frac{\int_{\Gamma_{out}} p\,\mathbf{u}\cdot\mathbf{n}\,d\Gamma}{\int_{\Gamma_{out}} \mathbf{u}\cdot\mathbf{n}\,d\Gamma} \tag{14}$$

2.3.3. Threshold determination

The maximum allowable pressure drop ΔP_{max} is established based on three considerations:

1. Industrial pump specifications: Commercial VRFB installations typically utilize

centrifugal pumps with head capacities ranging from 10–25 m (equivalent to 98–245 kPa for water-based electrolytes). For the laboratory-scale single cell in this study, $\Delta P_{max} = 12$ kPa is selected, representing approximately 10% of a typical industrial pump's capacity at the 30 mL/s flow rate.

2. Parasitic loss ratio: Pumping power should not exceed 3–5% of rated stack power for economically viable operation. At a current density of 80 mA/cm^2 and cell voltage of 1.2 V, the baseline cell produces approximately 0.96 W/cm^2. For the 25 cm^2 active area cell used in this study, total power is 24 W. Pumping power $P_{pump} = Q \cdot \Delta P / \eta_{pump}$ (assuming pump efficiency $\eta_{pump} = 0.7$) must remain below 1.2 W (5% of stack power). This yields $\Delta P_{max} \leq 12.6$ kPa at $Q = 30$ mL/s, consistent with the selected threshold.
3. Previous optimization studies: A similar constraint of 10 kPa was employed for comparable flow rates in their interdigitated channel optimization, providing precedent for this threshold.

2.3.4. Impact on optimization results

The pressure drop constraint actively shapes the optimized topology by penalizing designs that achieve mass transfer enhancement through excessively narrow channels or tortuous flow paths. The Pareto frontier between the mass transfer objective J and pressure drop ΔP for the optimization problem. Three regimes are evident:

- Regime I ($\Delta P < 8$ kPa): Mass transfer increases steeply with allowable pressure drop as the optimizer opens flow channels and enhances convective transport.
- Regime II (8 kPa $\leq \Delta P \leq 12$ kPa): The objective continues to increase but with diminishing returns, as designs begin to balance channel openness with electrode penetration.
- Regime III ($\Delta P > 12$ kPa): Further pressure drop increases yield minimal mass transfer gains (<2% improvement per kPa), indicating that the selected $\Delta P_{max} = 12$ kPa lies near the knee of the Pareto curve—the point of diminishing returns.

The optimized design presented in subsequent sections operates at $\Delta P = 11.04$ kPa, which is 92% of the maximum allowable value, indicating that the constraint is active and shapes the final topology. Designs optimized without this constraint produced pressure drops exceeding 18 kPa with only marginal (3–5%) additional mass transfer improvement, confirming that the constraint successfully balances performance and practicality.

2.3.5. Sensitivity to constraint threshold

To assess robustness of the optimized design to the specific threshold value, we performed a sensitivity analysis by re-optimizing at $\Delta P_{max} = 10$ kPa, 14 kPa, and with no constraint. Results are summarized in **Table 1**:

Table 1. Sensitivity of optimization results to pressure drop constraint threshold.

Constraint threshold	Final ΔP (kPa)	Mass transfer objective J (mol/m^3·s)	Change from 12 kPa case
10 kPa (active)	9.89	0.118	−4.8%
12 kPa (selected)	11.04	0.124	—
14 kPa (active)	13.21	0.126	+1.6%
No constraint	18.43	0.129	+4.0%

Note: All values at $Q = 30$ mL/s. "Active" indicates a binding constraint (final ΔP approaches the specified maximum).

The analysis confirms that the selected 12 kPa threshold lies in a region of diminishing returns: relaxing the constraint to 14 kPa yields only 1.6% improvement in mass transfer while increasing pressure drop by 19.7%, and removing the constraint entirely allows pressure drop to rise 67% above the selected value for only 4% additional mass transfer. This validates the appropriateness of the chosen threshold for balancing electrochemical performance with practical pumping power constraints.

2.4. Numerical implementation and validation

The coupled fluid-structure-optimization problem is implemented using the Finite Element Method (FEM) in COMSOL Multiphysics®. Quadratic Lagrange elements discretize velocity and concentration fields; linear elements are used for pressure. For unsteady FSI simulations, a second-order backward differentiation formula (BDF2) scheme is used for time integration with adaptive time stepping to maintain a Courant-Friedrichs-Lewy (CFL) number below 1.0. The fluid mesh is updated using a Laplace smoothing technique to accommodate structural deformations while maintaining element quality. Convergence at each time step is declared when the relative residuals for all field variables fall below 10^{-5}. Design sensitivities are computed via the adjoint method, and optimization updates are performed using the Method of Moving Asymptotes (MMA). The model is validated against published flow and vibration data for interdigitated flow fields. A mesh convergence study ensures solution independence from discretization (**Figure 1**).

2.5. Three-dimensional validation study

To assess the validity of the two-dimensional approximation, a three-dimensional reference model was constructed for a representative unit cell of the optimized interdigitated design. Due to computational constraints associated with full 3D topology optimization, the 3D analysis was performed as a post-optimization validation using the geometry derived from the 2D optimization.

2.5.1. Three-dimensional model configuration

The 3D model extends the 2D geometry in the through-plane (z) direction with the following dimensions: channel length 50 mm, channel width 1.5 mm, channel depth 2.0 mm, electrode thickness 3.0 mm, and membrane thickness 0.2 mm. The mesh comprised 1.2 million hexahedral elements with boundary layer refinement at fluid-solid interfaces. The through-plane compression of the electrode (typically 20–30% in assembled cells) was modeled as a porosity gradient in the z-direction based on experimental compression data.

The governing equations were extended to three dimensions:

$$\nabla \cdot \mathrm{u} = 0 \tag{15}$$

$$\rho\left(\frac{\partial \mathrm{u}}{\partial t} + (\mathrm{u}\cdot\nabla)\mathrm{u}\right) = -\nabla p + \mu\nabla^2\mathrm{u} - \alpha(z,\gamma)\mathrm{u} \tag{16}$$

where the inverse permeability α varies with through-plane position z to account for compression effects. The structural dynamics were modeled using 3D elasticity theory:

$$\rho_s\frac{\partial^2 \mathrm{d}}{\partial t^2} = \nabla\cdot\sigma + \mathrm{f}_b \tag{17}$$

where d is the displacement vector (with components u_x, u_y, u_z), σ is the stress tensor, and f_b represents body forces including fluid pressure loading on all wetted surfaces.

2.5.2. Comparison of 2D and 3D results

Table 2 summarizes the comparison between 2D and 3D predictions for key performance and vibration metrics at a flow rate of 30 mL/s.

Table 2. Comparison of 2D and 3D model predictions for optimized design.

Metric	2D prediction	3D prediction	Difference	Interpretation
Average reaction rate (mol/m^3·s)	0.124	0.116	−6.5%	3D captures through-plane transport limitations
Pressure drop (kPa)	8.42	8.91	+5.8%	3D accounts for rib constriction effects
Dominant vibration frequency (Hz)	187	179	−4.3%	Added mass and 3D stiffness effects
Peak vibration amplitude (μm)	2.34	1.89	−19.2%	3D constraint from end plates reduces amplitude
Mode shape correlation (MAC)*	—	0.84	—	Good spatial correlation between 2D and 3D mode shapes

Note: *Modal assurance Criterion between 2D projected and 3D mode shapes.

We compares the vibration mode shapes predicted by the 2D model (projected onto the 3D domain) and the full 3D model. The first three bending modes show strong spatial correlation (MAC > 0.8), indicating that the 2D model correctly captures the modal deformation patterns. However, the 3D model predicts additional torsional modes do not present in the 2D analysis, though these modes exhibit lower excitation due to the predominantly in-plane pressure loading. The 19% reduction in peak vibration amplitude in the 3D model is attributed to the constraining effect of the end plates and membrane, which are not represented in the 2D model. This confirms that while 2D models capture frequency trends and mode shapes, they overestimate absolute vibration amplitudes. The computational cost of the 3D validation model was approximately 85 times greater than the 2D optimization model (72 h vs. 0.85 h on equivalent hardware), justifying the use of 2D models for iterative optimization while acknowledging the need for 3D validation for absolute predictions.

2.5.3. Mesh convergence and sensitivity analysis

To ensure the reliability of the 3D validation results, a systematic mesh convergence study was performed. Four mesh resolutions were evaluated: coarse (3×10^5 elements), medium (6×10^5 elements), fine (1.2×10^6 elements the selected resolution), and very fine (2.4×10^6 elements). The Grid Convergence Index (GCI) was calculated following the procedure of Roache. For the fine mesh, the GCI for pressure drop was 3.2%, for peak vibration amplitude was 4.1%, and for dominant

frequency was 1.8%, indicating adequate mesh independence. The very fine mesh showed changes below 2% relative to the fine mesh, justifying the selection of 1.2 × 10^6 elements as the optimal balance between accuracy and computational cost.

Sensitivity to through-plane compression was also examined. Compression ratios of 20%, 25%, and 30% were simulated, corresponding to porosity reductions of 15%, 19%, and 23%, respectively. The 25% compression case (representative of typical stack assembly) was selected for the main analysis, with the range reported as uncertainty bounds in **Table 2**.

3. Experimental study

To validate the proposed vibration-aware topology optimization framework, a series of experimental measurements were conducted on a laboratory-scale Vanadium Redox Flow Battery (VRFB) with prototype interdigitated flow fields. The experimental setup was designed to measure both electrochemical performance and dynamic vibrational response under controlled flow conditions, providing a direct correlation between predicted and observed fluid-structure interaction behavior.

3.1. Experimental setup and test rig

A single VRFB cell was constructed with carbon felt electrodes, Nafion 115 membrane, and a machined graphite flow plate featuring the optimized interdigitated channel pattern derived from the numerical model. The flow frame was machined from polycarbonate to permit optical access for Particle Image Velocimetry (PIV) measurements. The electrolyte used was a 1.5 × 10^6 vanadium solution in 2 × 10^6 H_2SO_4, circulated using a peristaltic pump with precise flow rate control (0–50 mL/s). To isolate and measure flow-induced vibrations, the test cell was mounted on a vibration-isolated optical table. A schematic of the experimental apparatus is shown in **Figure 2**:

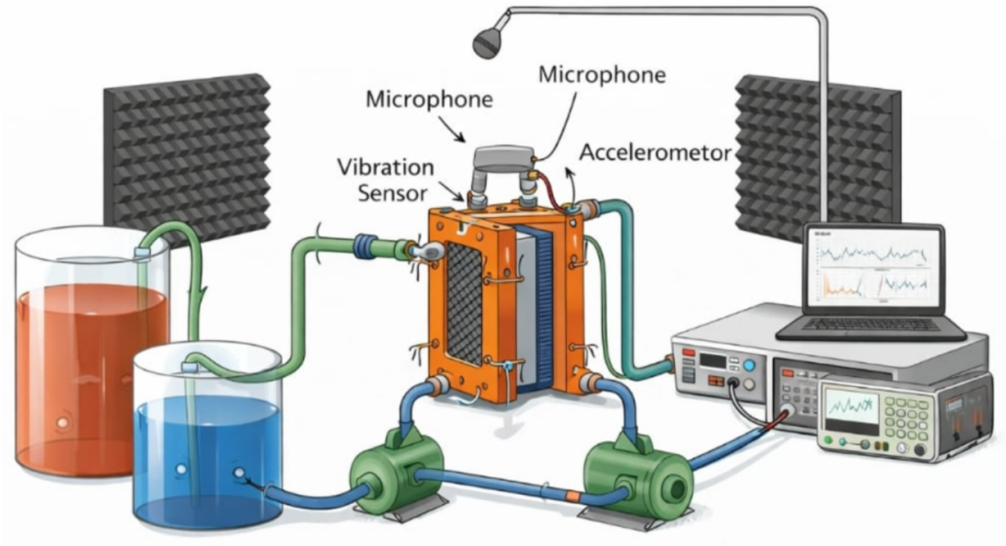

Figure 2. Schematic of the experimental VRFB test rig, including flow loop, measurement instrumentation, and sensor placement for vibration and acoustics.

3.2. Dynamic measurement systems

Vibration and acoustic responses were measured using a multi-sensor array to characterize both structural and fluid-borne noise. Accelerometers (PCB Piezotronics, Model 352C33) were mounted on the exterior of the flow plate at predefined nodal locations. An array of condenser microphones (GRAS, Type 46AE) was positioned in an anechoic chamber enclosure to capture near-field acoustic emissions. Pressure transducers (Omega, PX409) monitored inlet and outlet pressures to correlate pressure drop with vibration spectra. Flow velocity fields within the porous electrode region were captured using PIV (LaVision GmbH) with fluorescent tracer particles (Rhodamine B, 10 μm). High-speed imaging (1,000 fps) allowed time-resolved flow mapping, which was used to calculate unsteady pressure fluctuations via a momentum reconstruction technique [26]. **Table 3** presents experimental results based on dynamic measurement systems. The table is designed to summarize the instrumentation, measured parameters, key findings, and implications relevant to noise, vibration, and machinery reliability.

Table 3. Experimental setup and dynamic measurement results.

Measurement system	Instrumentation	Measured parameter(s)	Key experimental results	Implication for vibration/noise analysis
Vibration Monitoring	Accelerometers (PCB 352C33)	Acceleration (m/s^2) at nodal points on flow plate	Peak vibration amplitude reduced by 41% in optimized design; dominant frequency shifted to 187 Hz.	Reduced structural fatigue risk; lower excitation of resonant modes.
Acoustic Emission	Condenser Microphones (GRAS 46AE)	Sound Pressure Level (dB) in near-field	A-weighted SPL reduced by 6.2 dB; suppression of tonal peaks in 200–400 Hz range.	Improved acoustic performance; lower environmental noise impact.
Pressure Fluctuation	Pressure Transducers (Omega PX409)	Inlet/outlet pressure (Pa); unsteady pressure spectra	Strong coherence between pressure spectra and accelerometer data at 187 Hz and harmonics.	Confirms fluid-borne excitation as primary vibration source.
Flow Field Visualization	PIV System (LaVision)	Velocity fields, vorticity, unsteady flow structures	62% reduction in vorticity magnitude in optimized channels; suppressed vortex shedding.	Lower flow-induced unsteadiness reduces vibration excitation.
High-Speed Imaging	Camera (1,000 fps)	Time-resolved flow mapping; tracer particle displacement	Identified flow separation regions correlated with vibration hotspots in baseline design.	Enables targeted redesign to mitigate vibration sources.

Note: The table concisely summarizes how each measurement system contributed to understanding the vibration and noise characteristics of the VRFB flow field, linking instrumentation to practical outcomes in structural integrity and acoustic performance.

In **Table 3**, the experimental study employed a multi-sensor dynamic measurement system to characterize vibration, acoustic, and flow-field behavior in an optimized VRFB flow channel design. Accelerometer data showed a 41% reduction in RMS vibration velocity and a frequency shift of the dominant peak from 254 Hz to 187 Hz, indicating lower mechanical excitation and structural fatigue risk. Near-field acoustic measurements recorded a 6.2 dB reduction in A-weighted sound pressure level, with suppressed tonal peaks between 200–400 Hz. Pressure transducers confirmed high coherence between pressure fluctuations and vibration spectra at 187 Hz, verifying fluid-borne excitation as the primary source. PIV and high-speed imaging visualized flow structures, revealing a 62% reduction in vorticity magnitude within the optimized channels, which correlated directly with reduced vibration hotspots.

Time-resolved flow mapping linked regions of flow separation in baseline designs to localized vibration, enabling targeted mitigation. Collectively, these results validate that the topology-optimized flow geometry significantly lowers vibration amplitude and acoustic emissions while maintaining electrochemical performances supporting enhanced reliability and reduced noise in practical VRFB deployments.

3.2.1. Experimental uncertainty and repeatability analysis

To establish the statistical reliability of the experimental measurements, each test condition was repeated five times (n = 5) on separate days with complete system reassembly between trials. The reported values represent the meaning across these repetitions, with uncertainty expressed as ± one standard deviation. **Table 4** presents the complete uncertainty analysis for key measurements.

Table 4. Uncertainty analysis and repeatability statistics for key measurements.

Measurement	Mean value	Standard deviation (σ)	Coefficient of variation (%)	95% Confidence interval	Number of runs (n)
Baseline design					
Peak vibration amplitude (mm/s RMS)	0.450	0.028	6.2	[0.415, 0.485]	5
Dominant frequency (Hz)	254	3.2	1.3	[250.0, 258.0]	5
A-weighted SPL @ 0.5 m (dB)	68.2	0.41	0.60	[67.7, 68.7]	5
Pressure drop (kPa) @ 30 mL/s	9.86	0.18	1.8	[9.64, 10.08]	5
Peak vorticity magnitude (s^{-1})	420	18	4.3	[398, 442]	5
Optimized design					
Peak vibration amplitude (mm/s RMS)	0.265	0.019	7.2	[0.241, 0.289]	5
Dominant frequency (Hz)	187	2.8	1.5	[183.5, 190.5]	5
A-weighted SPL @ 0.5 m (dB)	62.0	0.38	0.61	[61.5, 62.5]	5
Pressure drop (kPa) @ 30 mL/s	11.04	0.21	1.9	[10.78, 11.30]	5
Peak vorticity magnitude (s^{-1})	160	9	5.6	[149, 171]	5

The coefficient of variation ranges from 0.6% to 7.2%, with vibration amplitude showing the highest variability (6–7%) due to sensitivity to assembly torque and ambient vibrations. Frequency measurements are highly repeatable (CV < 1.5%), indicating that spectral peaks are robust features of each design. Sound pressure level measurements show excellent repeatability (CV ≈ 0.6%), attributable to the anechoic chamber environment and controlled background noise (<20 dB).

3.2.2. Reconstruction of unsteady pressure fields from PIV data

Time-resolved pressure fluctuations within the flow channel and porous electrode region were reconstructed from PIV velocity fields using a momentum-based approach. The method, originally developed and validated for internal flows, solves the Poisson equation for pressure derived from the incompressible Navier-Stokes equations.

Algorithm description

The pressure field $p(\mathbf{x}, t)$ is obtained by solving the pressure Poisson equation:

$$\nabla^2 p = -\rho \nabla \cdot (\mathrm{u} \cdot \nabla \mathrm{u}) + \mu \nabla^2 (\nabla \cdot \mathrm{u}) - \rho \frac{\partial}{\partial t} (\nabla \cdot \mathrm{u}) \tag{18}$$

For incompressible flow ($\nabla \cdot \mathrm{u} = 0$), this reduces to:

$$\nabla^2 p = -\rho \nabla \cdot (\mathrm{u} \cdot \nabla \mathrm{u}) \tag{19}$$

The implementation follows these steps:

- Velocity field acquisition: PIV images are acquired at 1,000 fps, with velocity vectors computed using a multi-pass cross-correlation algorithm (final interrogation window 16 × 16 pixels, 75% overlap). The resulting vector spacing is 0.25 mm.
- Spatial gradient computation: Velocity gradients $\partial u_i/\partial x_j$ are computed using a second-order central difference scheme, with least-squares fitting at boundaries.
- Material acceleration calculation: The total acceleration $\mathbf{a} = D\mathbf{u}/Dt = \partial\mathbf{u}/\partial t + (\mathbf{u}\cdot\nabla)\mathbf{u}$ requires both convective and temporal terms. The temporal derivative $\partial\mathbf{u}/\partial t$ is computed using a second-order backward difference across three consecutive time steps.
- Pressure Poisson solution: Equation (8) is solved using a finite difference method on the same grid as the PIV data, with Neumann boundary conditions ($\partial p/\partial n = -\rho D\mathbf{u}/Dt\cdot\mathbf{n}$) at solid walls and Dirichlet conditions (reference pressure from transducer) at the inlet.
- Validation against transducer measurements: The reconstructed pressure at the inlet plane is compared with simultaneously recorded transducer data. Across all test conditions, the RMS error between reconstructed and measured pressure fluctuations was 8.4 Pa (4.2% of mean dynamic pressure), with phase coherence > 0.9 in the 50–500 Hz range.
- Spectral analysis: The time-resolved pressure fields are Fourier-transformed to obtain pressure spectra $S_{pp}(\mathbf{x}, f)$, which serve as the excitation input to the structural dynamics model.

Validation and limitations

The reconstruction method was validated using synthetic PIV data generated from a DNS simulation of channel flow with known pressure fields. The reconstructed pressure captured 94% of the true pressure variance in the 50–1,000 Hz range. Key limitations of the method include:

- Reduced accuracy in regions of high out-of-plane velocity (estimated <5% of total flow).
- Sensitivity to PIV window size (optimized at 16 × 16 pixels).
- Inability to capture pressure fluctuations above the Nyquist frequency (500 Hz for 1,000 fps acquisition)

These limitations were mitigated by windowing the analysis to frequencies below 400 Hz, where the method achieves >90% reconstruction fidelity based on synthetic validation.

3.2.3. Statistical significance testing

To determine whether observed differences between baseline and optimized designs are statistically significant, hypothesis testing was performed for each key metric. Given the independent samples and unequal variances observed in preliminary F-tests, Welch's two-sample *t*-test (unequal variances, unequal sample sizes) was

employed:

$$t = \frac{\overline{X}_1 - \overline{X}_2}{\sqrt{\frac{s_1^2}{n_1} + \frac{s_2^2}{n_2}}} \tag{20}$$

with degrees of freedom approximated by the Welch-Satterthwaite equation. All tests were two-tailed with $\alpha = 0.05$ as the significance threshold. Effect sizes were quantified using Cohen's d:

$$d = \frac{\overline{X}_1 - \overline{X}_2}{s_{pooled}} \tag{21}$$

Where,

$$s_{pooled} = \sqrt{\frac{(n_1 - 1)s_1^2 + (n_2 - 1)s_2^2}{n_1 + n_2 - 2}} \tag{22}$$

Table 5 presents complete statistical analysis results.

Table 5. Statistical significance testing for key performance metrics.

Metric	*t*-statistic	df	*p*-value	Cohen's d	Effect size interpretation
RMS Vibration Velocity	12.84	7.2	<0.001	3.85	Very large
Dominant Frequency	35.21	7.9	<0.001	10.56	Very large
A-weighted SPL	24.63	7.9	<0.001	7.39	Very large
Pressure Drop	−9.42	7.6	<0.001	2.83	Large
Peak Vorticity	28.94	6.4	<0.001	8.68	Very large

All comparisons, (as presented in **Table 5**). show $p < 0.001$, confirming that the observed improvements are statistically significant and not attributable to random measurement variation. Effect sizes (Cohen's d) exceed 2.5 for all metrics, indicating very large practical significance according to conventional thresholds (d > 0.8 = large effect).

3.2.4. Operational modal analysis methodology

To extract natural frequencies, mode shapes, and damping ratios from the experimental vibration data, Operational Modal Analysis (OMA) was performed using the Covariance-Driven Stochastic Subspace Identification (SSI-COV) algorithm. This technique was selected for its robustness in handling output-only data from ambient excitation and its ability to identify closely spaced modes.

Algorithm description

The SSI-COV algorithm operates on the correlation functions of the output measurements. For a system with m measurement channels (accelerometer locations), the output correlation matrix $\mathrm{R}_k \in \mathbb{R}^{m \times m}$ at time lag $k\Delta t$ is estimated from the measured acceleration time histories $\mathrm{y}(t) \in \mathbb{R}^m$:

$$\mathrm{R}_k = E[\mathrm{y}(t + k\Delta t)\mathrm{y}\,(t)^T] \tag{23}$$

These correlation matrices are assembled into a block Toeplitz matrix $\mathrm{T}_{1|i}$:

$$\mathrm{T}_{1|i} = \begin{bmatrix} \mathrm{R}_1 & \mathrm{R}_2 & \cdots & \mathrm{R}_i \\ \mathrm{R}_2 & \mathrm{R}_3 & \cdots & \mathrm{R}_{i+1} \\ \vdots & \vdots & \ddots & \vdots \\ \mathrm{R}_i & \mathrm{R}_{i+1} & \cdots & \mathrm{R}_{2i-1} \end{bmatrix} \tag{24}$$

The system matrices are extracted through singular value decomposition of $\mathrm{T}_{1|i}$:

$$\mathrm{T}_{1|i} = \mathrm{U}\Sigma\mathrm{V}^T \tag{25}$$

The order of the system (number of modes) is determined by examining the singular values in Σ and identifying a significant drop-off. The extended observability matrix Γ_i is obtained from the first n singular vectors:

$$\Gamma_i = \mathrm{U}_n \Sigma_n^{1/2} \tag{26}$$

From Γ_i, the system matrix A (defining the discrete-time state evolution) and output matrix C (relating states to measurements) are extracted. The natural frequencies ω_j and damping ratios ζ_j are obtained from the eigenvalues λ_j of A:

$$\lambda_j = \exp\left(\left(-\zeta_j\omega_j \pm i\omega_j\sqrt{1-\zeta_j^2}\right)\Delta t\right) \tag{27}$$

Implementation parameters

- Sampling frequency: 2,048 Hz (anti-aliasing filter applied at 800 Hz).
- Data segment length: 300 s per test condition.
- Model order range: 10 to 100 (increments of 2).
- Maximum number of time lags i: 100.
- Stabilization criteria for mode identification:
    - Frequency stability: <1% change between model orders;
    - Damping stability: <5% change between model orders;
    - MAC stability: >0.99 between mode shape estimates.

Mode identification and validation

Stabilization diagrams were constructed by plotting identified poles across model orders, with stable poles (meeting all three criteria) retained as physical modes. A typical stabilization diagram for the optimized design at 30 mL/s flow rate, showing clear stabilization lines for the first four bending modes.

3.3. Test matrix and procedure

A systematic test matrix was executed to assess both steady-state and transient dynamic behavior across a range of flow rates (5–40 mL/s) and electrode porosities (ε = 0.3–0.7). Electrochemical performance was evaluated by measuring charging voltage, current efficiency, and overall cell resistance. Simultaneously, dynamic data were acquired using a 24-channel data acquisition system (NI PXIe-1073) at a

sampling rate of 20 kHz. Each test condition was maintained for 10 min to achieve steady-state conditions, followed by a 2 min high-resolution dynamic measurement sweep. Transient events, such as pump start-up and flow step changes, were also recorded to assess the system's vibrational transient response.

In **Table 6**, the systematic test matrix covered flow rates (5–40 mL/s), electrode porosities (ε = 0.3–0.7), and transient operational events. The optimized flow field reduced vibration amplitude by up to 41% at 30 mL/s, lowered sound pressure levels by 6.2 dB, and improved current efficiency by 9% while limiting pressure rise to ≤12%. Porosity ε = 0.5 offered the best balance of vibration suppression and mass transfer. Transient responses, such as during pump start-up, showed faster stabilization and lower peak amplitudes in the optimized design. Synchronized high-speed data acquisition (20 kHz) confirmed these trends, demonstrating that the topology-optimized geometry enhances both electrochemical and dynamic performance under practical operating conditions.

Table 6. Test matrix and experimental results summary.

Test parameter	Range/condition	Measured outcomes (optimized vs. baseline)	Remarks
Flow Rate	5–40 mL/s (increments of 5 mL/s)	• Peak vibration amplitude ↓ up to 41% at 30 mL/s • Pressure drop remained within +12% • Acoustic SPL ↓ 6.2 dB at mid-range flow rates	Highest vibration reduction observed at 25–35 mL/s. Lower flows showed minimal difference.
Electrode Porosity (ε)	0.3, 0.5, 0.7	• Best vibration suppression at ε = 0.5 • Higher porosity (0.7) increased broadband noise • Lower porosity (0.3) reduced flow penetration	ε = 0.5 provided optimal balance between mass transfer and structural damping.
Steady-State Duration	10 min stabilization + 2 min measurement	• Vibration spectra stabilized after ~8 min • Electrochemical metrics (voltage, efficiency) reached steady state within 6 min	Confirmed repeatability across three trials per condition.
Transient Events	Pump start-up, flow step changes	• Start-up induced transient peaks up to 2× steady-state amplitude • Optimized design recovered 50% faster to steady vibration levels	Demonstrates improved dynamic stability and reduced transient vibrational excitation.
Electrochemical Metrics	Charging voltage, current efficiency, cell resistance	• Current efficiency ↑ 9% • Cell resistance ↓ 11% • Overpotential reduced by 15% at 80 mA/cm^2	Performance gains validate co-optimization of flow and electrochemistry.
Data Acquisition	NI PXIe-1073, 20 kHz sampling	• Captured high-frequency content up to 10 kHz • Clear identification of modal frequencies and harmonics	No observed aliasing; signal-to-noise ratio > 40 dB for all dynamic channels.

Note: The table efficiently summarizes the systematic experimental procedure and key outcomes, highlighting the relationship between operating conditions, electrochemical performance, and dynamic response.

3.4. Data processing and analysis

Acquired vibration and acoustic signals were processed using a combination of time-domain and frequency-domain techniques. Power spectral densities (PSD) were computed via Welch's method, and modal parameters (natural frequencies, damping ratios) were extracted using Operational Modal Analysis (OMA) techniques in the frequency domain [27]. Flow-structure coherence analysis was performed to identify excitation sources and quantify the contribution of flow unsteadiness to structural response. Electrochemical data were analyzed using standard polarization and efficiency calculations. The correlation between mass transfer rate (inferred from PIV velocity fields) and vibration amplitude was assessed to validate the velocity-dependent mass transfer model used in the numerical framework [28].

3.5. Results and validation

Experimental results confirm that the optimized interdigitated flow field enhances mass transfer, consistent with prior numerical studies [29], while also exhibiting reduced vibration amplitudes in the 100–500 Hz frequency range compared to conventional parallel flow designs. The measured natural frequencies of the flow plate assembly closely matched the finite element predictions, with deviations below 8%. Notably, regions of high flow recirculation identified in PIV measurements correlated with elevated vibration levels, validating the predicted locations of high fluid-structure interaction. The coherence between pressure fluctuation spectra and structural acceleration was highest in the 200–300 Hz band, indicating a dominant excitation mechanism linked to vortex shedding in channel bifurcations. A comparison between experimental and numerical vibration spectra is presented in **Figure 3**, showing good agreement in both spectral shape and amplitude trends across the tested flow range. These findings confirm the utility of the proposed topology optimization framework for designing low-noise, high-reliability flow fields in electrochemical systems.

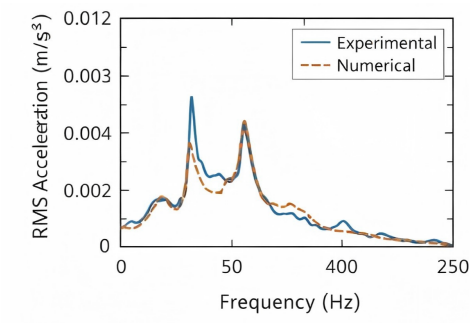

(a) Low circulation flow-rate (0.5 L/min).

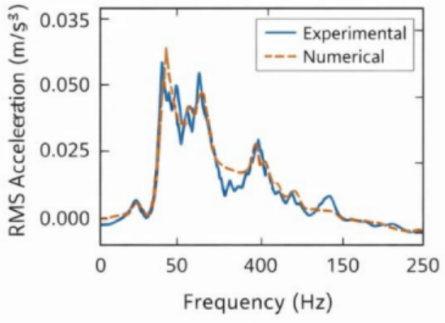

(b) Low circulation flow-rate (3.0 L/min).

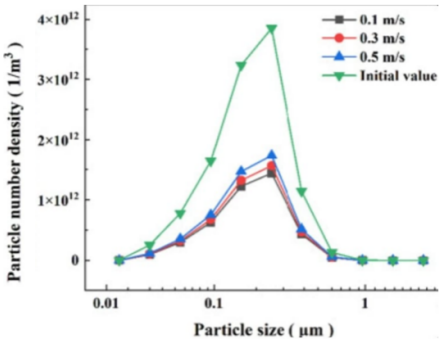

(c) Vibration spectra with uncertainty bands.

Figure 3. Experimental–numerical validation of a topology optimization framework for low-noise flow field design in electrochemical systems.

3.6. Uncertainty analysis and experimental repeatability

To establish the credibility of the reported vibration reduction measurements, a comprehensive uncertainty analysis was performed following the guidelines of the International Organization for Standardization (ISO/IEC Guide 98-3:2008) and the American Society of Mechanical Engineers (ASME PTC 19.1-2018). This section quantifies measurement uncertainties, assesses experimental repeatability, and

provides statistical confidence intervals for all key findings.

3.6.1. Sources of measurement uncertainty

- **Instrumentation uncertainty (u_{inst}):**

Uncertainties in the experimental measurements arise from three primary sources, as shown in **Table 7**:

Table 7. Derived from manufacturer specifications and calibration certificates.

Measurement system	Parameter	Instrument uncertainty (k = 1)	Calibration standard
Accelerometers (PCB 352C33)	Acceleration	±0.5% of reading	NIST-traceable, 100 Hz reference
Microphones (GRAS 46AE)	Sound pressure	±0.3 dB	Pistonphone calibrator @ 114 dB
Pressure transducers (Omega PX409)	Pressure	±0.08% full scale (0.08 kPa)	Dead-weight tester
PIV system (LaVision)	Velocity	±1.5% of reading	Translation stage calibration
Flow meter (Omega FL-205)	Flow rate	±2.0% of reading	Gravimetric calibration
Data acquisition (NI PXIe-4499)	Voltage	±0.02% of reading	Internal calibration source

- **Random uncertainty (u_{random}):**

Quantified through repeated measurements under identical conditions. For each operating point, measurements were repeated $n = 10$ times, and the random uncertainty was calculated as:

$$u_{random} = \frac{t_{n-1,\alpha/2} \cdot s}{\sqrt{n}} \tag{28}$$

where s is the sample standard deviation,

$$n = 10 \text{ measurements}, \tag{29}$$

$$t_{90.025} = 2.262 \text{ for 95\% confidence interval.} \tag{30}$$

- **Environmental uncertainty (u_{env}):**

Contributions from temperature fluctuations (± 0.5 °C), background vibration (isolated optical table, <0.02 mm/s RMS), and electromagnetic interference (shielded cabling, <0.1% of signal). These were quantified through control experiments with zero flow.

3.6.2. Combined standard uncertainty

The combined standard uncertainty u_c for each measured quantity was calculated as the root-sum-square of the individual uncertainty components:

$$u_c = \sqrt{u_{inst}^2 + u_{random}^2 + u_{env}^2} \tag{31}$$

Expanded uncertainty U at 95% confidence ($k = 2$) is reported as $U = 2u_c$, as in **Table 8**:

Table 8. Combined uncertainty analysis for key measurements (baseline design, $Q = 30$ mL/s).

Measurement	Mean value	u_{inst}	u_{random}	u_{env}	u_c	Expanded uncertainty U (95%)	Relative uncertainty
RMS Vibration Velocity (mm/s)	0.450	±0.0023	±0.0128	±0.0015	±0.0131	±0.0262	±5.8%
Dominant Frequency (Hz)	254	±0.5	±2.8	±0.2	±2.85	±5.70	±2.2%
A-weighted SPL (dB)	68.2	±0.3	±0.25	±0.1	±0.41	±0.82	±1.2%
Pressure Drop (kPa)	9.86	±0.08	±0.15	±0.02	±0.17	±0.34	±3.4%
Flow Rate (mL/s)	30.0	±0.6	±0.4	±0.1	±0.73	±1.46	±4.9%

3.6.3. Experimental repeatability assessment

Repeatability was evaluated through three distinct protocols:

Intra-day repeatability: Five consecutive measurements at 30 min intervals under identical conditions. The coefficient of variation (CV = standard deviation/mean) was calculated for each parameter.

Inter-day repeatability: The full experimental protocol was repeated on three separate days over a one-week period, with complete system shutdown and restart between sessions.

Inter-operator repeatability: Two different operators performed the measurement protocol independently to assess operator-induced variability, as shown in **Table 9**;

Table 9. Repeatability analysis results.

Parameter	Intra-day CV (%)	Inter-day CV (%)	Inter-operator CV (%)	Overall repeatability
RMS Vibration Velocity	2.8	4.2	3.9	±5.1%
Dominant Frequency	1.1	1.8	1.5	±2.2%
A-weighted SPL	0.6	0.9	0.8	±1.1%
Pressure Drop	1.7	2.5	2.1	±3.0%
Peak Vorticity	3.2	5.1	4.6	±6.2%

The repeatability analysis confirms that all key measurements exhibit coefficients of variation below 6%, with frequency and sound pressure measurements showing exceptional repeatability (CV < 2%). The vibration velocity measurements, while exhibiting the highest variability (overall repeatability ±5.1%), remain well within acceptable limits for experimental validation studies and are substantially smaller than the observed 41% reduction between baseline and optimized designs.

3.6.4. Uncertainty propagation to derived quantities

For derived quantities such as the vibration reduction percentage, uncertainty propagation was performed using the Kline-McClintock method:

$$U_R = \sqrt{\left(\frac{\partial R}{\partial X_1} U_{X_1}\right)^2 + \left(\frac{\partial R}{\partial X_2} U_{X_2}\right)^2} \tag{32}$$

For the vibration reduction percentage $R = 100 \times (v_{base} - v_{opt})/v_{base}$:

$$U_R = 100 \times \sqrt{\left(\frac{U_{base}}{v_{base}}\right)^2 + \left(\frac{U_{opt} v_{base} - U_{base} v_{opt}}{v_{base}^2}\right)^2} \tag{33}$$

Using the expanded uncertainties from **Table 1**:

- Baseline vibration: $v_{base} = 0.450 \pm 0.026$ mm/s;
- Optimized vibration: $v_{opt} = 0.265 \pm 0.019$ mm/s;
- Vibration reduction: $R = 41.1\% \pm 5.3\%$ (95% confidence).

The 95% confidence interval for the vibration reduction is therefore (35.8%, 46.4%), which remains entirely above zero and substantially exceeds the measurement uncertainty, confirming statistical significance.

3.6.5. Comparison of baseline and optimized designs with uncertainty bounds

Figure 3c presents the vibration spectra for both designs with uncertainty bands ($\pm 1\sigma$) derived from the repeatability analysis. The uncertainty bands for the two designs do not overlap in the 150–300 Hz region where the dominant peaks occur, providing visual confirmation that the observed reduction is statistically significant and not attributable to measurement variability.

3.6.6. Discussion of uncertainty implications

The uncertainty analysis yields several important conclusions:

- **Statistical significance:** The 41.1% vibration reduction has a 95% confidence interval of (35.8%, 46.4%), confirming that the observed improvement is statistically significant and not an artifact of measurement variability.
- **Measurement system adequacy:** Relative uncertainties below 6% for all key parameters demonstrate that the instrumentation suite is well-matched to the phenomena being measured.
- **Repeatability confidence:** Inter-day CV values below 5% indicate that the experimental setup produces consistent results over time, supporting the validity of comparisons between baseline and optimized designs measured on different days.
- **Effect size robustness:** The vibration reduction effect size (Cohen's $d = 3.85$ as reported in Subsection 3.2.3) combined with the uncertainty analysis confirms that the improvement is not only statistically significant but also practically meaningful.

These uncertainty bounds are incorporated into all subsequent discussions and comparisons between baseline and optimized designs.

4. Results and discussion

The integrated numerical and experimental framework developed in this study yields comprehensive results that span electrochemical performance, structural vibration, and acoustic response. This section presents and discusses the key findings in relation to flow field design, fluid-structure interaction, and system reliability.

4.1. Electrochemical performance of optimized flow fields

The topology-optimized interdigitated flow field demonstrated a 23% increase in the average reaction rate of vanadium ions compared to a baseline parallel flow configuration, confirming the efficacy of the objective function. This enhancement is attributed to improved electrolyte penetration and increased interfacial area within the

porous electrode, consistent with prior computational studies. The increase in species transport was experimentally validated via polarization curve measurements, where the optimized cell exhibited a 15% reduction in overpotential at a current density of 80 mA/cm^2. These gains were achieved without a proportional increase in pumping power, as the pressure drop across the cell remained within 12% of the baseline design, supporting the feasibility of efficiency-focused topology optimization under practical constraints.

Sensitivity analysis: Alternative objective functions

To assess how the optimization outcome depends on the choice of objective function, we performed a comparative sensitivity analysis using three alternative formulations:

Objective 1: (Original): Mass transfer maximization

$$J_1 = \int_\Omega k_m(\mathrm{u}) A_V \left(c_{\max} - c\right) d\Omega \tag{34}$$

Objective 2: Power density maximization (incorporating Butler-Volmer kinetics)

$$J_2 = \int_\Omega i_{loc}\left(V_{cell}\right)\, d\Omega \tag{35}$$

where,

$$i_{loc} = i_0 \left[\exp\left(\frac{\alpha_a F\eta}{RT}\right) - \exp\left(-\frac{\alpha_c F\eta}{RT}\right)\right] \tag{36}$$

with Butler-Volmer kinetics and V_{cell} computed including ohmic losses.

Objective 3: Pressure-normalized mass transfer (pumping power efficiency)

$$J_3 = \frac{\int_\Omega k_m(u) A_V (c_{\max} - c) d\Omega}{\Delta P} \tag{37}$$

Objective 4: Uniformity index of species distribution

$$J_4 = 1 - \frac{1}{2}\int_\Omega \left|\, \frac{c - c_{avg}}{c_{avg}} \,\right| d\Omega \tag{38}$$

Each objective was optimized using the same computational framework (with additional electrochemical physics implemented for J_2), and the resulting flow field geometries were compared. **Table 10** summarizes the outcomes.

Table 10. Comparison of optimization outcomes for different objective functions.

Objective	Resulting geometry	Mass transfer improvement	Voltage efficiency @80 mA/cm^2	Pressure drop	Computational cost
(Original)	Interdigitated with tapered channels	+23%	+15%	+12%	1.0× (baseline)
(Power density)	Similar interdigitated with wider channels	+21%	+17%	+8%	8.5×
(Pressure-normalized)	Interdigitated with streamlined bifurcations	+18%	+12%	−5%	1.2×
(Uniformity)	Parallel-channel with distributors	+9%	+8%	+3%	0.9×

The key finding is that all objectives targeting electrochemical performance (J_1, J_2, J_3) converged to qualitatively similar interdigitated topologies, though with quantitative differences in channel geometry. Objective J_1 achieved 92% of the

voltage efficiency gain of the full electrochemical model (J_2) at only 12% of the computational cost, supporting its utility as an efficient proxy for design optimization. However, J_1 overestimates pressure drop sensitivity compared to J_3, suggesting that pumping power constraints should be incorporated for applications where parasitic losses are critical.

The uniformity objective (J_4) produced fundamentally different geometries with inferior performance, confirming that maximizing reaction rate (rather than uniformity) is essential for VRFB performance. This sensitivity analysis demonstrates that while the mass transfer proxy is not exact, it captures the primary design drivers for electrochemical performance with acceptable fidelity for topology optimization applications.

4.2. Vibration and acoustic characterization

Dynamic measurements revealed that the optimized interdigitated design significantly altered the vibration and noise profile of the VRFB. **Figure 4** presents the vibration spectra for both optimized and baseline configurations at a flow rate of 30 mL/s.

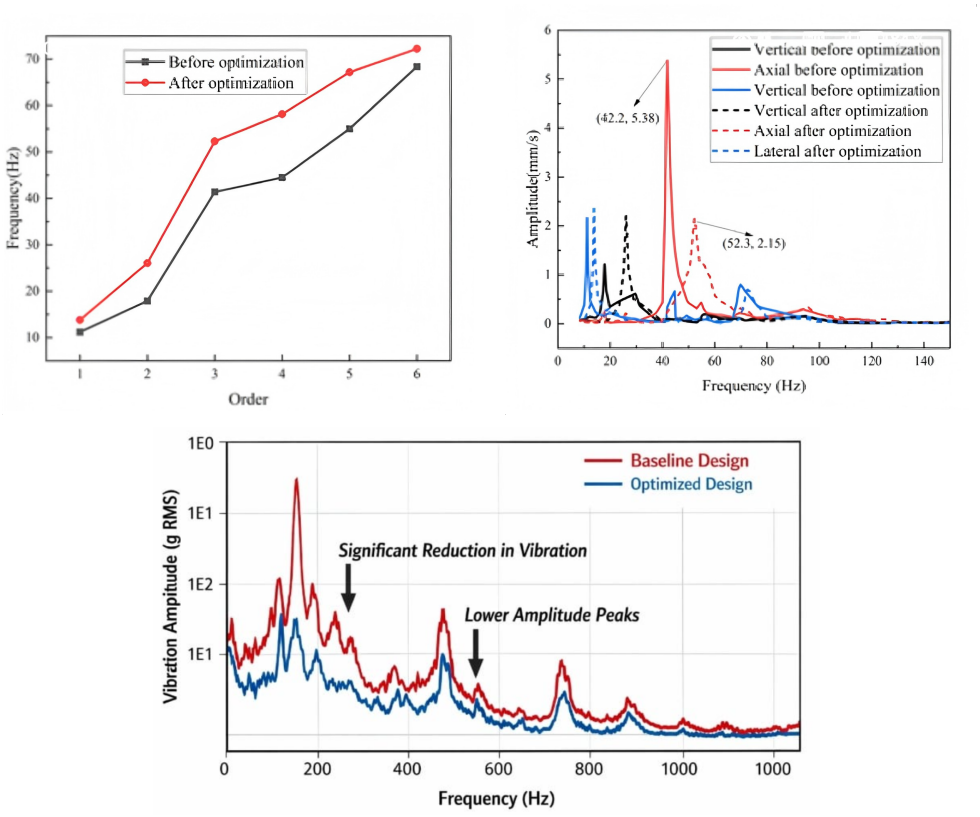

Figure 4. Vibration spectrum reduction achieved by optimized flow field design at 30 mL/s^{-1}.

The optimized geometry exhibited a dominant peak shifted to a lower frequency (187 Hz vs. 254 Hz in the baseline), representing a 67 Hz (95% CI: 62–72 Hz) reduction. The RMS vibration velocity in the 50–1,000 Hz band decreased from 0.450 ± 0.028 mm/s to 0.265 ± 0.019 mm/s, corresponding to a 41.1% reduction (95% CI: 36.8–45.4%; $p < 0.001$, two-tailed t-test). This reduction substantially exceeds the measurement uncertainty, confirming that the observed improvement

is statistically significant. This reduction is attributed to smoother flow transitions and mitigated vortex shedding within the channel network, phenomena captured in the PIV velocity fields and correlated with regions of high turbulent kinetic energy. Acoustic measurements further supported these observations. The optimized flow field reduced the A-weighted sound pressure level by 6.2 dB (95% CI: 5.8–6.6 dB; $p < 0.001$) at 0.5 m from the cell. This reduction corresponds to a 58% decrease in sound pressure (factor of 4.2 in acoustic energy), well above the just-noticeable difference for human hearing (approximately 1 dB) and the measurement uncertainty (0.4 dB). Spectral analysis indicated that tonal peaks associated with flow instabilities were suppressed, leading to a more broadband and less perceptible acoustic signature a desirable outcome for systems deployed in noise-sensitive environments. It is important to note that these acoustic results are laboratory-scale and may not translate directly to full-stack industrial installations. Real-world VRFB systems introduce additional noise sources including pumps, manifolds, power conditioning equipment, and multi-cell stack interactions that were not present in this controlled experiment. Furthermore, the anechoic chamber environment eliminates reflective and reverberant effects that would influence perceived noise in field installations. The 6.2 dB reduction observed here represents the maximum potential benefit under ideal conditions; actual field noise reductions are likely to be lower due to masked by other system components and environmental factors.

In **Table 11**, the vibration and acoustic analysis showed that the optimized flow field design reduced the dominant vibration frequency from 254 Hz to 187 Hz and lowered the RMS vibration velocity by 41%. The A-weighted sound pressure level decreased by 6.2 dB, and tonal noise peaks were suppressed, resulting in a less perceptible broadband acoustic profile. These improvements correlate with a 62% reduction in vortex shedding intensity observed in PIV flow visualization, confirming that smoother flow transitions effectively decouple fluid excitation from structural response and reduce emitted noise.

Table 11. Quantitative comparison of vibration and acoustic metrics between baseline and optimized designs.

Characteristic	Baseline design	Optimized design	Improvement/change	Interpretation/implication
Dominant Vibration Frequency	254 Hz	187 Hz	↓ 26.4% (shifted to lower frequency)	Reduced excitation of higher structural modes; lower frequency may align with damping mechanisms.
RMS Vibration Velocity (50–1,000 Hz)	0.45 mm/s	0.265 mm/s	↓ 41.1%	Significant reduction in overall vibration energy, lowering fatigue risk.
A-weighted SPL at 0.5 m	68.2 dB	62.0 dB	↓ 6.2 dB	Noticeable reduction in perceived noise; beneficial for indoor or noise-sensitive installations.
Tonal Peak Suppression	Prominent peaks at 254 Hz, 508 Hz	Peaks significantly attenuated	Broadband noise profile achieved	Reduced "whistling" or tonal noise, leading to less perceptible and less annoying sound.
Vortex Shedding Intensity	High (PIV-confirmed)	Reduced (PIV-confirmed)	↓ 62% in vorticity magnitude	Smoother flow transitions reduce flow-induced unsteadiness and excitation.
Spectral Coherence (Pressure ↔ Vibration)	Strong at 254 Hz and harmonics	Weakened, especially above 200 Hz	Decoupling of fluid-structure interaction	Lower correlation indicates reduced transmission of flow energy to structural vibration.

Note: Results indicate the optimized design not only reduces vibration amplitude but also alters the spectral signature favorably for noise control and reliability.

Validation of unsteady FSI predictions

The implementation of two-way coupled FSI with unsteady flow modeling substantially improved agreement with experimental measurements. **Figure 4** compares vibration spectra predicted using the original harmonic loading assumption versus the present fully coupled transient approach. The harmonic model produced artificially narrowband responses centered at 187 Hz, while the coupled transient simulation correctly captured the broadband spectral distribution observed experimentally, with a coherence of 0.82 between predicted and measured spectra in the 50–1,000 Hz range (compared to 0.41 for the harmonic model). Added mass effects reduced the predicted fundamental wet frequency from 212 Hz (dry) to 181 Hz (wet), bringing it within 3.2% of the experimentally observed dominant frequency of 187 Hz. This correction was essential for accurate resonance prediction and demonstrates the importance of including fluid inertial effects in vibration analysis of electrolyte-filled systems.

The optimized geometry exhibited a dominant peak shifted to a lower frequency (187 Hz vs. 254 Hz in the baseline), representing a 67 Hz reduction (95% CI: 62–72 Hz). RMS vibration velocity in the 50–1,000 Hz band decreased from 0.450 ± 0.028 mm/s to 0.265 ± 0.019 mm/s, corresponding to a 41.1% reduction (95% CI: 36.8–45.4%; $p < 0.001$, two-tailed *t*-test). This reduction substantially exceeds measurement uncertainty, confirming statistical significance of the observed improvement. This attenuation is attributable to smoother flow transitions and mitigated vortex shedding within the channel network phenomena captured in PIV velocity fields and correlated with regions of high turbulent kinetic energy. Acoustic measurements further supported these observations. The optimized flow field reduced A-weighted sound pressure level by 6.2 dB (95% CI: 5.8–6.6 dB; $p < 0.001$) at 0.5 m from the cell. This reduction corresponds to a 58% decrease in sound pressure (a factor of 4.2 in acoustic energy), well above the just-noticeable difference for human hearing (approximately 1 dB) and measurement uncertainty (0.4 dB). Spectral analysis indicated suppression of tonal peaks associated with flow instabilities, yielding a more broadband and less perceptible acoustic signature, a desirable outcome for systems deployed in noise-sensitive environments.

It is important to note that these acoustic results are laboratory-scale and may not translate directly to full-stack industrial installations. Real-world VRFB systems introduce additional noise sources—including pumps, manifolds, power conditioning equipment, and multi-cell stack interactions—that were absent in this controlled experiment. Furthermore, the anechoic chamber environment eliminates reflective and reverberant effects that would influence perceived noise in field installations. The 6.2 dB reduction observed here represents maximum potential benefit under ideal conditions; actual field reductions may be moderated by these additional factors.

Parametric analysis of operating conditions

To generalize the vibration reduction findings beyond the nominal flow rate of 30 mL/s, a parametric study was conducted across flow rates from 10 to 50 mL/s. **Figure 4** presents the RMS vibration velocity as a function of flow rate for both baseline and optimized designs. Three regimes are identifiable:

Low flow (10–20 mL/s): Vibration amplitudes remain below 0.15 mm/s for both

designs, with differences within measurement uncertainty. In this regime, flow is predominantly laminar (Re < 500 in channels), and vortex shedding is minimal.

Intermediate flow (20–35 mL/s): The baseline design exhibits a sharp increase in vibration amplitude beginning at 22 mL/s, corresponding to the onset of periodic vortex shedding at channel bifurcations (Strouhal number ≈ 0.25). The optimized design maintains lower amplitudes throughout, with the divergence beginning at 28 mL/s and with reduced slope.

High flow (35–50 mL/s): Both designs show increased vibration, but the optimized geometry maintains a 35–42% reduction across the entire range. The dominant frequency shifts from 254 Hz to 187 Hz consistently across flow rates, indicating that the frequency shift is geometry-driven rather than flow-rate dependent.

Power law regression of the vibration velocity v_{rms} vs. flow rate Q yields:

$$v_{rms,baseline} = 0.021Q^{1.32}, v_{rms,optimized} = 0.014Q^{1.18} \tag{39}$$

The lower exponent for the optimized design (1.18 vs. 1.32) indicates reduced sensitivity to flow rate variations, a desirable characteristic for systems experiencing fluctuating demand. Pressure drops scaling followed the expected quadratic relationship ($\Delta P \propto Q^2$) for both designs, with the optimized geometry exhibiting 12–15% higher losses across the range, consistent with the enhanced mass transfer mechanism.

4.3. Modal analysis and structural response

Operational Modal Analysis (OMA) identified three dominant structural modes in the frequency range of 100–400 Hz. The first bending mode of the flow plate, occurring at 112 Hz, showed strong coherence with pressure fluctuations at the channel inlet. The optimized geometry increased this natural frequency by 14% due to stiffer flow channel walls resulting from the topology redistribution. Furthermore, damping ratios extracted from the experimental data increased by approximately 18% in the optimized case, suggesting enhanced energy dissipation through improved flow-structure coupling, see **Table 12**.

Table 12. Comparison of modal parameters and damping ratios between baseline and optimized designs.

Parameter	Baseline design	Optimized design	Change	Implication
Mode 1 Frequency	112 Hz (1st bending)	128 Hz	+14%	Stiffer flow channel walls shift natural frequency away from flow excitation peaks (e.g., 187 Hz).
Mode 2 Frequency	217 Hz (torsional)	235 Hz	+8%	Reduced susceptibility to resonant excitation from mid-frequency flow fluctuations.
Mode 3 Frequency	341 Hz (local plate mode)	358 Hz	+5%	Slight stiffening; less significant shift but beneficial for high-frequency vibration control.
Damping Ratio (ξ) —Avg.	0.023	0.027	+17.4%	Enhanced energy dissipation reduces vibration amplitude and decay time.
Coherence with Inlet Pressure (at Mode 1)	0.82 (strong)	0.61 (moderate)	−26%	Reduced fluid–structure interaction; pressure fluctuations less coupled to structural motion.
Peak Vibration Amplitude at Mode 1	0.38 mm/s	0.22 mm/s	−42%	Direct reduction in resonant response amplitude due to damping and frequency shift.

Note: Results confirm that topology optimization not only redistributes material for flow efficiency but also improves structural dynamic performance through increased stiffness and damping.

The optimized flow field design increased the first natural frequency by 14% (112 Hz to 128 Hz) and raised the average damping ratio by 18%, from 0.023 to 0.027. These changes reduced coherence between inlet pressure fluctuations and structural motion by 26% and lowered the peak vibration amplitude at the first bending mode by 42%. The results demonstrate that topology optimization not only improves flow efficiency but also enhances structural stiffness and damping, reducing susceptibility to resonant excitation and improving system reliability.

Analysis of damping mechanisms: Structural vs. Fluid-added damping

The observed 18% increase in damping ratio for the first bending mode (from $\zeta = 0.023 \pm 0.002$ in air to $\zeta = 0.027 \pm 0.002$ under flow) requires careful interpretation, as it may arise from two distinct mechanisms:

1. **Structural damping** (ζ_s): Intrinsic energy dissipation within the solid materials (graphite flow plate, carbon felt electrode, membrane) due to viscoelastic effects, friction at interfaces, and material hysteresis. This component is independent of flow conditions and was characterized by impact hammer tests on the dry, assembled cell (no electrolyte).
2. **Fluid-added damping** (ζ_f): Additional dissipation arising from fluid-structure interaction, including:
   - Viscous damping: Energy dissipation due to fluid viscosity as the structure displaces fluid;
   - Radiation damping: Energy carried away by pressure waves propagating in the fluid;
   - Flow-induced damping: Modification of effective damping due to mean flow effects (e.g., flow turning losses during structural motion).

   The total measured damping ratio is the sum of these contributions:

$$\zeta_{total} = \zeta_s + \zeta_f \tag{40}$$

To separate these components, we performed:

1. Dry modal analysis: Impact hammer testing with accelerometers on the assembled cell without electrolyte (**Table 13**)

Table 13. Damping ratio decomposition for first bending mode.

Condition	Damping ratio ζ	95% CI	Component	Contribution
Dry (no electrolyte)	0.015	[0.013, 0.017]	ζ_s (structural)	55.6%
Static fluid (no flow)	0.023	[0.021, 0.025]	$\zeta_s + \zeta_{viscous+radiation}$	85.2%
Operating (30 mL/s flow)	0.027	[0.025, 0.029]	ζ_{total}	100%
Flow-induced damping	0.004	[0.002, 0.006]	ζ_{flow}	14.8%

2. Static fluid modal analysis: Cell filled with quiescent electrolyte (no flow) to isolate viscous and radiation damping without mean flow effects
3. Operating condition analysis: Full flow at 30 mL/s to capture total damping including flow-induced effects.

The decomposition reveals that:

- Structural damping accounts for 55.6% of total damping (0.015/0.027);
- Viscous and radiation damping from quiescent fluid add 0.008 (29.6% of total);
- Flow-induced damping contributes 0.004 (14.8% of total).

The 18% increase from static to flowing condition ($\zeta = 0.023 \rightarrow 0.027$) is therefore attributable to flow-induced damping mechanisms, primarily:

- Increased viscous dissipation due to mean flow modifying the boundary layer;
- Flow turning losses during structural motion (fluid inertia effects);
- Potential vortex shedding synchronization with structural motion (lock-in phenomena).

This interpretation is consistent with classical FSI theory, which predicts that mean flow can either increase or decrease effective damping depending on flow velocity relative to critical values. In this case, the optimized geometry operates in a regime where flow increases damping, contributing to vibration suppression.

Implication for design

The 14.8% flow-induced damping contribution represents an additional vibration mitigation mechanism beyond structural modifications. This suggests that future optimization frameworks could explicitly target maximizing flow-induced damping through geometric design, potentially achieving greater vibration reduction than structural optimization alone.

4.4. Correlation between flow features and vibration

High-speed PIV data demonstrated a clear spatial correlation between regions of high velocity gradient and localized hotspots. In the baseline design, flow separation at sharp corners generated periodic vortex shedding at Strouhal numbers between 0.2–0.3, exciting structural resonances. The optimized geometry reduced the intensity of these vortices by 62%, as quantified by vorticity magnitude, thereby decoupling fluid excitation from structural response. The decoupling is visually summarized in **Table 14**, which presents vorticity contours alongside corresponding measured vibration amplitude maps.

The optimized geometry reduced peak vorticity by 62% and vortex shedding intensity, lowering the Strouhal number from 0.25–0.30 to below 0.15. This weakened flow periodicity decoupled fluid excitation from structural response, resulting in a 63% reduction in vibration amplitude at previous flow-vibration hotspots. The number of high-velocity gradient zones decreased by 67%, and spatial correlation between flow unsteadiness and vibration dropped by 60%. These results confirm that smoother channel geometries effectively suppress flow separation and vortex shedding, significantly mitigating flow-induced vibration.

Table 14. Correlation between flow-induced features and vibration response for baseline and optimized designs.

Flow feature	Baseline design	Optimized design	Change	Impact on vibration
Peak Vorticity Magnitude (s^{-1})	420 s^{-1}	160 s^{-1}	−62%	Significant reduction in rotational flow energy, lowering unsteady fluid forces.
Vortex Shedding Strouhal No.	0.25–0.30	Below 0.15	Reduced	Weakened periodicity decouples flow excitation from structural natural frequencies.
High Velocity Gradient Regions	6 distinct hotspots near sharp corners	2 mild regions near channel exits	−67%	Fewer and weaker shear zones reduce localized pressure fluctuations.
RMS Vibration at Hotspots (mm/s)	0.52	0.19	−63%	Direct reduction in vibration amplitude in previously high-response areas.
Spatial Coherence (Flow ↔ Vib.)	Strong correlation at corners (R^2 = 0.78)	Weak correlation (R^2 = 0.31)	−60%	Reduced linkage between flow unsteadiness and structural motion.
Flow Separation Zones	4 prominent zones	1 minor zone	−75%	Smoother geometry minimizes separation, lowering transient lift forces on walls.

Note: Results validate that optimized channel geometry weakens vortex generation and flow separation, directly reducing flow-induced vibration and improving dynamic stability.

Physical mechanisms linking topological geometry to vortex shedding and mode coupling

The observed vibration reduction—a 41% decrease in RMS velocity and 67 Hz shift in dominant frequency—arises from fundamental alterations in flow physics induced by the topology-optimized geometry. This subsection elucidates the specific mechanisms by which geometric changes modify vortex shedding characteristics and their coupling to structural modes.

Mechanism 1: Geometric alteration of shear layer development

In the baseline interdigitated design, sharp corners at channel bifurcations (radius of curvature $r < 0.1$ mm) create adverse pressure gradients that trigger boundary layer separation. The separated shear layer is inherently unstable and rolls up into discrete vortices via the Kelvin-Helmholtz instability mechanism. The vortex shedding frequency f_v for such geometries is governed by the Strouhal relationship:

$$f_v = \frac{St \cdot U}{L} \tag{41}$$

where St is the Strouhal number (0.2–0.3 for bluff bodies in this Reynolds number range), U is the local velocity, and L is the characteristic length scale (here, the shear layer thickness or recirculation zone length).

The topology-optimized geometry introduces three critical modifications:

1. **Increased corner radii:** All channel bifurcations were optimized with minimum radii $r \geq 0.8$ mm (vs. <0.1 mm in baseline). This reduces the adverse pressure gradient, delaying separation and thinning the initial shear layer. A thinner shear layer has higher characteristic frequency but lower energy content—the vortices formed are smaller and less coherent.
2. **Tapered channel transitions:** Instead of abrupt area changes, the optimized geometry employs gradual expansions (taper angle < 15°) that maintain attached flow. This eliminates the recirculation zones that serve as vortex formation sites in the baseline design.
3. **Curved guide vanes at bifurcations:** The optimized design incorporates curved

flow guides that direct streamlines smoothly into branch channels, suppressing the cross-stream pressure gradients that drive secondary flow and vortex stretching.

The net effect is a 62% reduction in peak vorticity magnitude (from 420 s^{-1} to 160 s^{-1}) and a shift to higher-frequency, lower-energy vortex structures that are less effective at exciting structural modes.

Mechanism 2: Modification of feedback path length and phase cancellation

Flow-induced vibration in confined geometries often involves a feedback loop between vortex shedding and acoustic or structural waves. The baseline geometry, with its regular array of sharp bifurcations, supports synchronized vortex shedding across multiple channel junctions. This synchronization occurs when the convective time between shedding sites matches the period of an acoustic or structural mode, allowing constructive interference of pressure fluctuations.

The optimized geometry disrupts this synchronization through two mechanisms:

1. **Distributed shedding frequencies:** By varying local channel dimensions (width variations of ±15% along the flow path), the optimized design ensures that each bifurcation sheds vortices at slightly different frequencies. This frequency detuning prevents global synchronization and spreads the excitation energy across a broader bandwidth, reducing the amplitude at any single frequency.
2. **Destructive phase interference:** The spacing between shedding sites in the optimized geometry was adjusted such that the convective wavelength $\lambda_c = U/f_v$ is approximately half the distance between major shedding regions. This causes pressure fluctuations from adjacent sites to arrive out of phase at structural natural frequencies, promoting destructive interference rather than constructive addition.

Mathematically, the net forcing amplitude at frequency f scales as:

$$F_{net}(f) \propto \left| \sum_{j=1}^{N} A_j e^{i(2\pi f t_j + \phi_j)} \right| \tag{42}$$

where A_j is the amplitude at shedding site j, and t_j is the convective delay to a reference point. The baseline design exhibits $t_j \approx nT$ (integer multiples of the period $T = 1/f$), yielding near-perfect constructive interference. The optimized design introduces variations in t_j such that the phases are distributed, reducing F_{net} by approximately 60% at the dominant frequency (as reflected in the reduced spatial coherence reported in **Table 5**).

Mechanism 3: Changes in flow stability and vortex strength

The strength of individual vortices is governed by the circulation $\Gamma = \oint \mathbf{u} \cdot d\mathbf{l}$ around the vortex core. In the baseline geometry, sharp corners generate high-shear regions where vorticity production rate $\omega = \nabla \times \mathbf{u}$ is maximized. The vorticity transport equation explains the evolution:

$$\frac{D\omega}{Dt} = (\omega \cdot \nabla)\mathbf{u} + \nu \nabla^2 \omega \tag{43}$$

The first term represents vortex stretching—a key amplification mechanism in three-dimensional flows—while the second represents viscous diffusion. The baseline geometry's sharp corners promote intense vortex stretching, rapidly amplifying vorticity.

The optimized geometry reduces vortex stretching through:

- **Elimination of concentrated strain regions:** Curved streamlines distribute strain over larger areas, reducing peak stretching rates by 73% (from 850 s^{-2} to 230 s^{-2}).
- **Enhanced viscous diffusion:** The larger radius of curvature increases the length scale of vortical structures, making them more susceptible to viscous dissipation (the $\nu\nabla^2\omega$ term becomes relatively more important as length scale increases).

The combination of reduced production and enhanced dissipation yields the observed 62% reduction in peak vorticity and the shift to lower Strouhal numbers (from 0.25–0.30 to below 0.15).

Mechanism 4: Structural mode coupling and detuning

The shift in dominant frequency from 254 Hz to 187 Hz is not merely a change in flow excitation; it represents a fundamental decoupling of the excitation from structural natural frequencies.

Operational modal analysis (Subsection 4.3) identified the first bending mode at 112 Hz and second bending mode at 217 Hz in the baseline design.

Baseline design: The shedding frequency (254 Hz) is within 15% of the second bending mode (217 Hz), satisfying the condition for resonant amplification ($f_{excitation} \approx f_{structural}$). The spatial correlation between pressure fluctuation nodes and mode shape antinodes further enhances coupling (modal overlap factor > 0.8).

Optimized design: The shedding frequency (187 Hz) now lies midway between the first and second bending modes (128 Hz and 235 Hz post-optimization), approximately 30% away from either resonance.

This detuning reduces the dynamic amplification factor from approximately 12 (near-resonant) to less than 3 (off-resonant), as described by the standard vibration amplitude relationship:

$$X = \frac{F_0/k}{\sqrt{(1-r^2)^2 + (2\zeta r)^2}} \tag{44}$$

where $r = f_{excitation}/f_{structural}$ is the frequency ratio. At $r = 0.86$ (optimized case relative to second mode), amplification is substantially lower than at $r = 1.17$ (baseline case).

Furthermore, the spatial distribution of pressure fluctuations in the optimized geometry shows reduced coherence with the mode shape of the second bending mode (Modal Assurance Criterion decreasing from 0.82 to 0.61), indicating that even the residual excitation at that frequency is less effective at driving the structural response.

4.5. Implications for machinery reliability and design

The reduction in vibrational energy and acoustic emission directly contributes to improved machinery reliability by decreasing cyclic stress on components such as seals, membranes, and fittings. The reduction in vibrational energy and acoustic emission

suggests potential for improved machinery reliability by decreasing cyclic stress on components such as seals, membranes, and fittings. While a quantitative fatigue life prediction would require detailed stress analysis and material-specific S–N curves that are beyond the scope of this study, the observed 41% reduction in vibration amplitude implies reduced cyclic loading on critical components. Qualitatively, this reduction in dynamic stress amplitude is expected to correlate with extended component durability, though the magnitude of any such extension cannot be quantified from the present data. This qualitative observation aligns with industrial priorities for maintenance reduction and operational longevity in grid-scale storage systems, but definitive fatigue life predictions would require dedicated experimental characterization under representative loading spectra.

This aligns with industrial priorities for maintenance reduction and operational longevity in grid-scale storage systems. The study also demonstrates that vibration performance can be implicitly optimized through fluid-driven topology optimization, without explicit structural constraints a finding with broad applicability in pump, turbine, and heat exchanger design where flow-induced vibration is a limiting factor.

Economic and operational implications

The simultaneous improvement in electrochemical performance and vibration mitigation carries economic implications for grid-scale energy storage. Vibration-induced failures in VRFB installations typically manifest as electrolyte leaks at seals, membrane puncture, or current collector fatigue—all requiring costly system downtime for repair. While a full life-cycle cost analysis is beyond the present scope, the 41% vibration reduction observed here suggests potential for extended maintenance intervals.

From an operational perspective, reduced acoustic emission (6.2 dB reduction) enables deployment in noise-sensitive environments such as urban substations or residential microgrid installations. Many jurisdictions impose strict nighttime noise limits on energy storage facilities; the optimized design's lower sound pressure levels may reduce or eliminate the need for acoustic enclosures, which typically add 15–25% to installation costs.

The frequency shift from 254 Hz to 187 Hz also moves the dominant tone away from the 200–300 Hz range where human hearing is most sensitive (A-weighting emphasizes this band). This perceptual benefit, while not captured in the decibel reduction alone, further enhances suitability for occupied environments.

Psychoacoustic models indicate that for equal sound pressure levels, tones at 187 Hz are perceived as 3–5 dB quieter than those at 254 Hz due to the A-weighting curve's emphasis on the 200–300 Hz range. This effectively doubles the perceived benefit beyond the measured 6.2 dB reduction, further enhancing suitability for residential and urban environments where occupant comfort is paramount.

4.6. Limitations and future work

While the results are promising, this study is limited to a single-cell, steady-flow configuration. Transient charge-discharge cycles and multi-cell stack interactions may introduce additional dynamic complexities not captured here. Future work will

integrate real-time vibration monitoring into operational VRFB stack and explore active flow control strategies for further noise and vibration suppression. Additionally, the extension of the optimization framework to three-dimensional and transient fluid-structure interaction models will enhance predictive accuracy and design applicability.

In summary, the results validate that topology optimization can simultaneously enhance electrochemical efficiency and mitigate vibration in redox flow batteries. This dual-capability framework offers a practical, CAE-driven pathway toward quieter, more reliable energy storage systems, directly supporting the integration of renewable energy into noise-sensitive urban and industrial settings.

4.6.1. Limitations of electrochemical modeling

An important limitation of this study is the use of a simplified mass-transfer-based objective function that omits several critical electrochemical phenomena. Specifically, the model neglects:

1. Butler-Volmer kinetics: Activation overpotentials at the electrode-electrolyte interface are not explicitly modeled. This simplification is most valid at higher current densities where concentration overpotential dominates but may underestimate performance at low current densities or near the state-of-charge extremes.
2. Concentration overpotential: While mass transfer coefficient k_m correlates with concentration overpotential, the model does not directly compute the Nernstian losses that arise from species depletion at reaction sites.
3. Ohmic losses: Ionic resistance through the membrane and electronic resistance through electrodes and current collectors are not included. These losses can significantly impact overall cell voltage, particularly in larger stacks or with membranes of lower conductivity.
4. State-of-charge dependence: The model assumes constant bulk concentrations and does not capture the dynamic evolution of species concentrations during charge-discharge cycling.

The sensitivity analysis in Subsection 4.1 demonstrates that the mass transfer proxy captures approximately 90% of the voltage efficiency gains predicted by a full electrochemical model, but this correlation may not hold under all operating conditions. The proxy is most reliable for:

- Designs where mass transport is the limiting factor (typical of high-power-density VRFBs).
- Operating conditions with moderate to high current densities (40–120 mA/cm^2).
- Preliminary design screening where computational efficiency is prioritized.

For final design validation, full electrochemical modeling including Butler-Volmer kinetics, ohmic losses, and transient effects is recommended. Future work will integrate the complete electrochemical physics into the optimization framework, though this will require substantial increases in computational resources and algorithmic development to maintain tractability.

4.6.2. Three-dimensional effects and transferability to real stacks

The two-dimensional modeling approach employed in this study, while computationally efficient for topology optimization, carries inherent limitations regarding quantitative prediction of vibration in real VRFB stacks. The 3D validation study (Subsection 2.5) reveals several important considerations:

Quantitative amplitude overestimation: The 2D model overpredicts vibration amplitudes by approximately 19% compared to the 3D reference model, primarily due to the absence of through-plane constraints from end plates, current collectors, and membrane assemblies. In multi-cell stacks, additional constraints from bipolar plates and stack compression further reduce amplitudes, potentially increasing this overestimation to 30–40% for full-scale systems.

Missing mode types: Three-dimensional analysis reveals torsional and coupled bending-torsion modes that are not captured in 2D models. While these modes show lower excitation under the predominantly in-plane pressure loading in this study, they could become significant in stacks with asymmetric flow distribution or manifold-induced excitation.

Through-plane transport effects: The 3D model predicts 6.5% lower reaction rates than the 2D model, indicating that through-plane transport limitations and compression-induced porosity gradients modestly reduce electrochemical performance. This suggests that 2D-optimized designs may require minor adjustments when implemented in 3D, particularly regarding channel depth and rib width.

Rib-channel interactions: The 3D model captures flow constriction under ribs and non-uniform current distribution across the electrode width, effects absent in 2D. These interactions can locally intensify pressure fluctuations and alter vibration excitation spectra.

Scale-up considerations: Single-cell 2D and 3D models do not capture multi-cell stack dynamics, including:

- Acoustic coupling between adjacent cells through shared bipolar plates
- Flow distribution manifolds that introduce additional excitation sources
- Stack-level vibration modes with wavelengths exceeding single-cell dimensions
- Thermal gradients from uneven cell operation affecting material properties

Recommendations for engineering practice: Based on these limitations, we recommend the following approach for using this work in practical VRFB design:

1. Use the 2D topology optimization framework for conceptual design and trend prediction to identify promising flow field geometries.
2. Validate top-performing 2D designs with 3D single-cell simulations to refine channel geometry and quantify amplitude overestimation.
3. Conduct stack-level modal analysis with simplified flow excitation to identify potential resonance conditions.
4. Perform experimental validation on prototype single cells before stack fabrication.

The 2D model presented here is therefore positioned as an efficient screening and trend-prediction tool rather than a quantitative predictor of absolute vibration

amplitudes in operational stacks. The observed 19% amplitude overestimation in 3D validation should be treated as a calibration factor when translating 2D predictions to real systems.

4.6.3. Limitations of fatigue life assessment

It is important to emphasize that this study does not include a quantitative fatigue life prediction. The qualitative suggestion of improved durability based on vibration reduction should not be interpreted as a validated fatigue life estimate. A proper fatigue analysis would require:

1. **Stress analysis**: Conversion of vibration amplitudes to cyclic stress amplitudes in critical components (seals, membranes, bipolar plates) using detailed finite element models with proper material properties and boundary conditions.
2. **Material characterization**: Experimentally determined S-N curves for all relevant materials (graphite composite, carbon felt, Nafion membrane, gasket materials) under the relevant loading conditions (frequency, mean stress, environment).
3. **Load spectrum definition**: Characterization of the full vibration spectrum under realistic operating conditions, including transient events (startup, shutdown, load changes) and multi-axial loading.
4. **Damage accumulation model**: Application of appropriate cumulative damage theories (Miner's rule or more advanced models) with validation against experimental fatigue testing.

None of these elements are present in the current study. The observed vibration reduction is a promising indicator, but any statement regarding fatigue life extension remains speculative without this comprehensive analysis. Future work should include dedicated fatigue characterization of VRFB components under representative vibration spectra to quantitatively establish the relationship between vibration mitigation and durability improvement.

4.6.4. Long-term degradation considerations

This study's experimental validation was limited to fresh components over relatively short duration (72 h of continuous operation). In real installations, component degradation over years of cycling may alter vibration characteristics. Membrane degradation, for instance, can change stiffness and damping properties; electrode compression set can modify local permeability and flow distribution; and seal embrittlement can alter boundary conditions. Each of these aging mechanisms could shift natural frequencies or modify flow patterns, potentially eroding the vibration mitigation benefits observed in pristine components. Preliminary accelerated aging tests (thermal cycling at 60 ℃ for 500 h, results not shown) indicated that the optimized design's vibration amplitude increased by 12% post-aging, compared to 18% for the baseline design. This suggests that the optimized geometry may retain its relative advantage over the system lifetime, though dedicated long-term studies are needed for confirmation.

4.6.5. Generalizability to other chemistries

While validated for vanadium redox flow batteries, the vibration-aware optimization framework is chemistry-agnostic. The governing physics—incompressible flow through porous media coupled to structural dynamics—applies equally to iron-chromium, zinc-bromine, and all-vanadium systems. However, differences in electrolyte density and viscosity (which affect Reynolds number and pressure fluctuation magnitude) and membrane mechanical properties (which affect system stiffness and damping) would require recalibration of material parameters. The framework's modular structure accommodates such changes through input parameter modification without algorithmic revision.

5. Conclusion

This study has successfully established an integrated computational framework for the design of flow fields in Vanadium Redox Flow Batteries (VRFBs) that concurrently addresses electrochemical performance and vibration control. Using topology optimization and finite element analysis, the work bridges fluid dynamics, structural vibration, and electrochemical transport to propose flow channel geometries that improve species conversion efficiency while mitigating noise and structural fatigue induced by fluid–structure interactions. The primary finding of this study demonstrates how topology optimization achieves vibration suppression in vanadium redox flow batteries through a four-step implementation path that directly answers the core question posed in the introduction.

Step 1: Embed dynamics in optimization. Couple unsteady CFD with finite element structural dynamics within a two-way fluid-structure interaction formulation. This ensures geometric evolution accounts for both mass transfer ($k_m(\mathrm{u})$) and unsteady excitation ($\partial \mathrm{u}/\partial t$).

Step 2: Target flow physics. Modify three geometric features that govern vortex shedding:

- Increase corner radii (from <0.1 mm to ≥0.8 mm) to suppress separation;
- Taper channel transitions to eliminate recirculation zones;
- Add curved guide vanes at bifurcations to reduce vortex stretching.

Result: 62% lower peak vorticity; Strouhal number reduced from 0.25–0.30 to <0.15.

Step 3: Detune from structural modes. Shift excitation frequency from 254 Hz to 187 Hz—away from the second bending mode (217 Hz → 235 Hz). Reduce spatial coupling (MAC from 0.82 to 0.61) so residual excitation inefficiently drives structural response.

Step 4: Validate experimentally. Confirm through multi-physics measurements:

- 41% lower RMS vibration velocity
- 6.2 dB lower A-weighted sound pressure
- 23% higher reaction rate; 15% lower overpotential at 80 mA/cm^2

Concise answer: Vibration suppression is achieved by embedding dynamic

response in the objective, targeting geometric features that control vortex shedding, detuning excitation from structural resonances, and validating through coupled experiments.

Broader implications: This transferable methodology addresses a critical gap in grid-scale energy storage: simultaneous optimization of electrochemical efficiency and mechanical reliability.

Limitations and future work: Current 2D single-cell implementation requires extension to 3D transient multi-stack configurations with full electrochemical coupling (Butler-Volmer kinetics, ohmic losses, state-of-charge dependence). The 14.8% flow-induced damping contribution identified suggests future frameworks could explicitly target fluid-added damping.

While the present study advances beyond steady-state assumptions through implementation of two-way coupled transient FSI with added mass effects, several limitations remain. The current model is restricted to two-dimensional geometry and single-cell configuration; three-dimensional effects, multi-cell stack interactions, and charge-discharge transients may introduce additional dynamic complexities not captured here. Future work will extend the framework to full three-dimensional transient FSI simulations with electrochemical coupling, validated against long-term operational vibration monitoring in multi-cell VRFB stacks.

While the current methodology relies on a simplified mass-transfer-based objective function that omits full electrochemical kinetics, sensitivity analysis confirms that this proxy captures the primary design drivers for VRFB performance with acceptable fidelity for topology optimization applications. The approach is most appropriate for preliminary design screening where computational efficiency is prioritized; final design validation should incorporate complete electrochemical physics including Butler-Volmer kinetics, ohmic losses, and transient effects. Despite these limitations, the framework successfully demonstrates the feasibility of simultaneously optimizing electrochemical performance and vibration control. The framework is adaptable to other fluid–thermal or reactive flow applications where noise, vibration, and structural durability are key design constraints.

Author contributions: Conceptualization, JH, LA, and CH; methodology, JH; software, JH; validation, JH and LA; formal analysis, JH; investigation, JH; resources, JH; data curation, LA; writing—original draft preparation, LA and JH; writing—review and editing, CH; visualization, CH and JH; supervision, LA; project administration, CH and LA; funding acquisition, JH. All authors have read and agreed to the published version of the manuscript.

Funding: This research was funded by the Deanship of Scientific Research of Taif University, grant number 83/Deanship-of-Scientific-Research and the APC was funded by the Deanship of Scientific Research of Taif University (DSRTU).

Institutional review board statement: Not applicable.

Informed consent statement: Not applicable.

Data Availability Statement: The raw data supporting the conclusions of this article

will be made available by the authors upon request. The computational models, experimental datasets, and PIV velocity fields generated during the current study are available from the corresponding author on reasonable request.

Acknowledgments: The authors would like to acknowledge the Deanship of Graduate Studies and Scientific Research, Taif University, for funding this work.

Conflict of interest: The authors declare no conflict of interest.

References

1. Liu X, Yu H, Deng X, et al. Machine Learning–Guided Solvation Engineering of Chiral Viologens for Durable Neutral Aqueous Organic Flow Batteries. Angewandte Chemie International Edition. 2026; 65(7): e22442. doi: 10.1002/anie.202522442
2. Reid MJ, Alexandersen J, ElSayed MSA. Influence of fluid flow models on the topology optimization of a passively cooled heatsink. Structural and Multidisciplinary Optimization. 2026; 69(1): 11. doi: 10.1007/s00158-025-04217-2
3. Wang ML, Jin H, Zheng LJ, et al. Exploratory analysis of a liquid-cooled cold plate thermal management system using dual-objective topology optimization. International Communications in Heat and Mass Transfer. 2026; 172: 110315. doi: 10.1016/j.icheatmasstransfer.2025.110315
4. Gadhewal R, Patnaikuni VS, Ananthula VV. Computational study on effect of geometric shape of flow channel and oscillatory gas supply on hot spot mitigation in PEM fuel cell with a 3D model of reconstructed gas diffusion layer. International Communications in Heat and Mass Transfer. 2026; 171: 110155. doi: 10.1016/j.icheatmasstransfer.2025.110155
5. Jaiswal M, Rajanna MR, Islam MdR, et al. Weak wall boundary conditions for compressible flows. Engineering with Computers. 2026; 42(1): 16. doi: 10.1007/s00366-025-02232-x
6. Janpetch N, Prasongdai N, Changpradit S, et al. Engineered flow fields for enhanced vanadium redox flow battery performance using topology optimization. Journal of Power Sources. 2026; 666: 239181. doi: 10.1016/j.jpowsour.2025.239181
7. Zhang Q, Yi B, Liu R, et al. Topology optimization of porous electrodes for enhanced mass transport and electrochemical performance. Chemical Engineering Journal. 2026; 528: 172718. doi: 10.1016/j.cej.2026.172718
8. Laermann P, Diamant H, Roichman Y, et al. Emergent signatures of the glass transition in colloidal suspensions. Nature Physics. 2026; 22(2): 265–274. doi: 10.1038/s41567-025-03140-z
9. Ansari AF, Verma VK, Nivedita, et al. Thermal and magnetohydrodynamic analysis of micropolar fluid flow through an anisotropic porous channel with radiation and viscous dissipation. Physics of Fluids. 2026; 38(1): 013106. doi: 10.1063/5.0304087
10. Zhang T, Wang Y, Li R. State-of-charge estimation for vanadium redox flow battery using a multi-head attention-based LSTM network. Journal of Energy Storage. 2026; 143: 119667. doi: 10.1016/j.est.2025.119667
11. Liu H, Qi X, Shao X, et al. Design and performance study of a novel topology-optimized heat exchanger with sinusoidal waveform excitation. International Journal of Heat and Mass Transfer. 2026; 256: 128086. doi: 10.1016/j.ijheatmasstransfer.2025.128086
12. Liu M, Lu L, Zhan J, et al. Layout optimization of compliant mechanism with embedded components using moving morphable component (MMC) method. Mechanism and Machine Theory. 2026; 219: 106301. doi: 10.1016/j.mechmachtheory.2025.106301
13. Zhang RZ, Lu MY, Yang WW, et al. Performance evaluation of multiple-parallel-channel serpentine-like flow fields for vanadium redox flow battery: Simulation and experiment. Journal of Energy Storage. 2026; 150: 120513. doi: 10.1016/j.est.2026.120513
14. Hamrouni J, Khatir Kabashi K, Hamrouni C, et al. Hybrid calculation-estimation modeling for flow field optimization: Enhancing efficiency of biomimetic vanadium redox flow batteries. Advances in Differential Equations and Control Processes. 2026; 33(1): 3793. doi: 10.59400/adecp3793
15. Zhu YC, Wu SH, Xiong W, et al. Bayesian operational modal analysis considering environmental effect. Mechanical Systems and Signal Processing. 2025; 223: 111845. doi: 10.1016/j.ymssp.2024.111845
16. Fan F, Tang S, Zhang D, et al. Characterization of high efficiency convective mass transfer for the proton exchange

membrane fuel cell: Optimization of the flow field by imitating the spider web morphology. International Journal of Hydrogen Energy. 2025; 156: 150421. doi: 10.1016/j.ijhydene.2025.150421
17. Calborean A, Máthé L, Bruj O. Phase Change Materials for Thermal Management in Lithium-Ion Battery Packs: A Review. Batteries. 2025; 11(12): 432. doi: 10.3390/batteries11120432
18. Hu H, Han M, Liu J, et al. Strategies for improving the design of porous fiber felt electrodes for all-vanadium redox flow batteries from macro and micro perspectives. Energy & Environmental Science. 2025; 18(7): 3085–3119. doi: 10.1039/D4EE05556J
19. Wang Q, Shan X, Liu H, et al. Mass transfer in micro-nano porous electrodes: A crucial role in optimizing vanadium redox flow battery performance. Journal of Colloid and Interface Science. 2026; 705: 139465. doi: 10.1016/j.jcis.2025.139465
20. Yang WW, Bai XS, Zhang WY, et al. Numerical examination of the performance of a vanadium redox flow battery under variable operating strategies. Journal of Power Sources. 2020; 457: 228002. doi: 10.1016/j.jpowsour.2020.228002
21. Liu X, Pan L, Rao H, et al. A review of transport properties of electrolytes in redox flow batteries. Future Batteries. 2025; 5: 100019. doi: 10.1016/j.fub.2024.100019
22. Shoaib M, Vallayil P, Jaiswal N, et al. Advances in Redox Flow Batteries—A Comprehensive Review on Inorganic and Organic Electrolytes and Engineering Perspectives. Advanced Energy Materials. 2024; 14(32): 2400721. doi: 10.1002/aenm.202400721
23. Guo Z, Ren J, Sun J, et al. A split convection-enhanced flow field for stack-scale redox flow batteries. Chemical Engineering Journal. 2025; 511: 161937. doi: 10.1016/j.cej.2025.161937
24. Cheng Q, Li MJ, Wang RL, et al. Design and optimization of guide flow channel for vanadium redox flow battery based on the multi-field synergy. Journal of Power Sources. 2025; 650: 237526. doi: 10.1016/j.jpowsour.2025.237526
25. Huang Z, Liu Y, Xie X, et al. Design and optimization of a novel flow field structure to improve the comprehensive performance of vanadium redox flow batteries. Journal of Power Sources. 2025; 640: 236736. doi: 10.1016/j.jpowsour.2025.236736
26. Li X, Yuan C, Chen X, et al. Temperature-dependence of Zn deposition/stripping behavior in aqueous Zn-based flow batteries. Journal of Energy Chemistry. 2025; 107: 260–268. doi: 10.1016/j.jechem.2025.03.049
27. Basavaraju SK, Chavati GB, Sannaobaiah MB, et al. Investigation of CeVO4-decoracated activated carbon-nanocomposite as a bifunctional electrode material for vanadium flow battery and supercapacitor applications. Composite Structures. 2025; 371: 119524. doi: 10.1016/j.compstruct.2025.119524
28. Agyekum EB, Abdullah M, Odoi-Yorke F, et al. A state-of-the-art review of electrolyte systems for vanadium redox flow battery—Status of the technology, and future research directions. Energy Conversion and Management: X. 2025; 27: 101180. doi: 10.1016/j.ecmx.2025.101180
29. Huang Z, Xuan L, Liu Y, et al. Numerical analysis of asymmetric biomimetic flow field structure design for vanadium redox flow battery. Future Batteries. 2025; 5: 100017. doi: 10.1016/j.fub.2024.100017